Iiris Routa

Modelling droplet assisted capillary self-alignment of microchips on complex alignment patterns for hybrid microassembly

School of Electrical Engineering

Thesis submitted for examination for the degree of Master of Science in Technology
Espoo 23.5.2013

Thesis supervisor:

Assistant professor Quan Zhou

Aalto University
School of Electrical Engineering

AALTO UNIVERSITY
SCHOOL OF ELECTRICAL ENGINEERING

ABSTRACT OF THE
MASTER'S THESIS

Author: Iiris Routa

Title: Modelling droplet assisted capillary self-alignment of microchips on complex alignment patterns for hybrid microassembly

Date: 23.5.2013 Language: English Number of pages: 68

Department of Automation and Systems Technology

Professorship: Control Engineering Code: AS-74

Supervisor and instructor: Assistant Professor Quan Zhou

In microassembly, components are typically less than a millimetre in size, and accurate positioning is very important. Currently robotic pick-and-place machines are widely used for assembly, but their operation becomes inefficient when the components are scaled down, due to the trade-off between the speed and accuracy. Capillary self-alignment has been proposed to replace or act as part of the assembly process to make the assembly faster and more accurate, allowing lower costs and smaller components.

Normally the patterns used as reference for capillary self-alignment are circular or square shaped hydrophilic patterns on hydrophobic background. However, in real applications, there are more requirements for system design, such as electric contacts, fabrication methods etc. Therefore, alignment patterns can have more complicated shapes than previously studied, with e.g. segmented structures or imperfections from manufacturing defects. In this master's thesis, capillary self-alignment of microchips on complex alignment patterns is studied using numerical modelling methods.

This thesis studies wetting on segmented patterns, and provides a method to approximate suitable droplet volume for self-alignment on those patterns. Then the self-alignment performance on those patterns is studied, and maximum initial offset is shown to be the size of one pattern segment. A model for patterns with jagged edges is created to demonstrate that the alignment force is reduced due to imperfections in alignment pattern. In addition, a simulator for chip trajectory is developed, and conditions for successful self-alignment are studied. Part of the results are earlier published in [1].

Keywords: self-alignment, self-assembly, capillary force, microassembly, modelling

AALTO-YLIOPISTO
SÄHKÖTEKNIIKAN KORKEAKOULU

DIPLOMITYÖN
TIIVISTELMÄ

Tekijä: Iiris Routa

Työn nimi: Mikrosirun pisara-avusteinen itsekohdistuminen monimutkaisiin kohdistuskuvioihin, mallinnus hybridimikrokokoonpanoa varten

Päivämäärä: 23.5.2013 Kieli: Englanti Sivumäärä: 68

Automaatio- ja systeemitekniikan laitos

Professuuri: Systeemitekniikka Koodi: AS-74

Valvoja ja ohjaaja: Assistant Professor Quan Zhou

Teknologian kehitys kannettavissa laitteissa, kuten tableteissa, on tuonut uusia haasteita mikrokokoonpanolle, kun yhä pienempiä komponentteja liitetään yhteen kasvavalla tarkkuudella. Mitä suurempaa tarkkuutta kokoonpanolta vaaditaan, sitä hitaampaa komponentteja latovan robotin toiminnasta tulee. Itsekohdistumista voidaan käyttää hyväksi parantamaan laitteiden suoritustehoa, jolloin myös tuotteen hinta laskee.

Eräs itsejärjestymisen muoto on kapillaarinen itsekohdistuminen, jossa mikrosiru asettuu nestepisaran pintajännityksen avulla hydrofiilisen kohdistuskuvion päälle hydrofobisella alustalla. Yleensä nämä kuviot ovat joko ympyrän tai neliön muotoisia, mutta kokoonpanosovelluksissa käytettäville kuvioille voi olla muitakin vaatimuksia ja reunaehtoja, kuten sähköisen kontaktin muodostaminen tai valmistustekniikat. Tällöin kuvioista tulee monimutkaisempia, mikä tarkoitaa esimerkiksi moniosaista kuviota, joka muodostuu elektrodeista, tai virheitä kuvion muodossa. Tässä diplomityössä mallinnetaan numeerisin menetelmin mikrosirun pisara-avusteista itsekohdistumista monimutkaisiin kohdistuskuvioihin.

Diplomityössä kehitetään menetelmä pisaran sopivan tilavuuden arvioimiselle mallintamalla pisaran leviämistä neliosaiselle kohdistuskuviolle ja tutkitaan mikrosirun suurinta asentovirhettä, jonka pisara-avusteinen itsekohdistuminen kykenee korjaamaan. Lisäksi osoitetaan, että virheet kohdistuskuvioissa heikentävät kapillaarivoimaa, joka kohdistaa mikrosirun. Työssä toteutetaan myös simulaattori mikrosirun trajektorin laskemiseksi. Osa työn tuloksista on julkaistu aiemmin [1].

Avainsanat: Itsekohdistuminen, itsejärjestyminen, kapillaarivoima, mikrokokoonpano, mallinnus

Preface

In spring 2010, I applied for a summer job as a research assistant in the micro- and nanorobotics research group in the department of Automation and Systems Technology in the former Helsinki University of Technology. I got the job and soon I found myself intrigued by the micro world and its phenomena. Three years have passed, and now I'm finishing my master's thesis, based on the research I have done for the projects of our research team.

First, I wish to thank my supervisor Dr. Quan Zhou for his kind patience during the process that finally led to this thesis. His help and support has been invaluable, and he has also given me freedom to find my own path during this time. I'm also grateful for all the advice and help from our research team members, Bo Chang, Antti Virta and Ville Liimatainen. Special thanks to Dr. Veikko Sariola for guidance to the magical world of Surface Evolver.

In addition, I want to thank my family for the warm support during my studies.

Otaniemi, May 2013

Iiris Routa

Contents

Symbols and abbreviations

Symbols

A	surface area
E	energy
$\vec{F}, F$	restoring force
h	vertical distance between chip and the pattern
L	length of the pattern or chip edge
m	mass of the chip
S	surface
∂S	boundary of surface
V	volume
x, y	position of the chip
α	twist of the chip
γ	surface tension or surface energy
θ	contact angle of the liquid on surface
φ	angle of height step in surface topography

Operators

∇	gradient
$\measuredangle$	angle between vectors
$\frac{\partial}{\partial x}$	partial derivative with respect to x
$\iint_S$	integral over surface S
$\int_{\partial S}$	integral over boundary of S
Σ_i	sum over the index i

Abbreviations

BGA	ball grid array
DOF	degrees of freedom
(E)SEM	(environmental) scanning electron microscope
FEM	finite element method
LED	light-emitting diode
MEMS	microelectromechanical system
RFID	radio-frequency identification
SA	self-assembly
SAM	self-assembled monolayer

1 Introduction

Nowadays, electrical devices, such as mobile phones and tablets, have constantly increasing functionality and performance, and at the same time their thickness is continuously reducing. Similar trend is visible in all portable devices where smaller size is preferable, for example in personal medical care devices that can be used near the patient and even at home. Highly integrated systems with more intelligence are also emerging, with great potential in e.g. automating homes or increasing safety in vehicles.

This development of increasingly smaller devices with increasing amount of components, functionality and diversity is a challenge for robotic assembly. The requirement for very accurate assembly at high speed causes problems to the capability of machine vision and the accuracy of assembly robot. A novel approach to overcome the shortcomings of conventional robotic assembly is self-assembly, where the devices are designed so that they will assemble autonomously [2], [3]. Self-assembly is nature's solution for assembly of complicated molecules, such as proteins, and the same principles can be mimicked to technical assembly tasks. Self-assembly can also be combined with robotic assembly to achieve the benefits from both [4].

In small scales, different forces dominate compared to our daily life and experiences. Gravitation gets less and less significant, and other "sticky" forces become more and more effective. This can be observed for example in morning dew on grass, as in figure 1. If the water droplet grows too large, it drops, but as long as the size is small, adhesion force that binds the droplet to the grass leaf keeps it from falling. These sticky forces have been a challenge in microassembly, since they make it difficult to handle small microparts. On the other hand, these phenomena can also be exploited when they are used for self-assembly purposes.

Sometimes the droplet can attach leaves together, as in figure 1(b). The force that binds the leaves together is known as capillary force, which originates from the surface tension of the water. This force can be used in self-assembly to align microparts with each other, which is called capillary self-alignment. When a liquid droplet is placed between two identical microchips, the surface tension of the liquid draws them perfectly on top of each other. This allows for example stacking of multiple microchips with great accuracy, which is not always achievable using current robotic technology. Chips may also be aligned on patterned substrate, so that hydrophilic part on the hydrophobic background makes the droplet stay where the chip is wanted to be assembled.

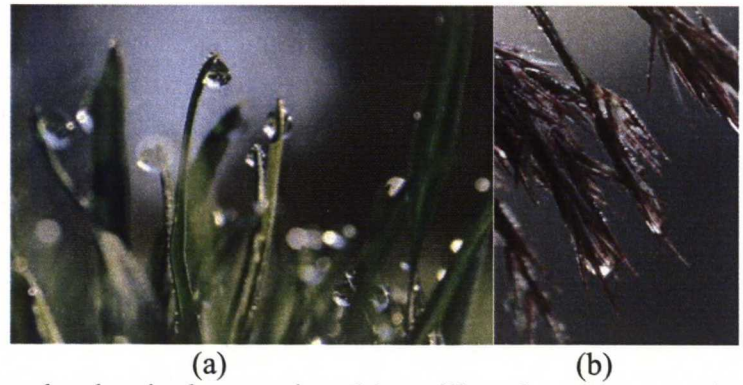

(a) (b)

Figure 1: Water droplets in the morning, (a) capillary force prevents the droplets from falling and (b) binds wet leaves together.

The objective of this master's thesis is to understand capillary self-alignment process for complex alignment patterns. Complex patterns refer to patterns that are different from conventional square and circular pattern shapes. For example, in RFID tag assembly, the assembly site has segmented pattern due to electrical contacts, which can be used also for alignment. In addition, fabrication of the patterns may result in defects in the patterns, and therefore the pattern definition is impaired. The illustration of self-alignment experiment on poorly defined jagged pattern is shown in figure 2.

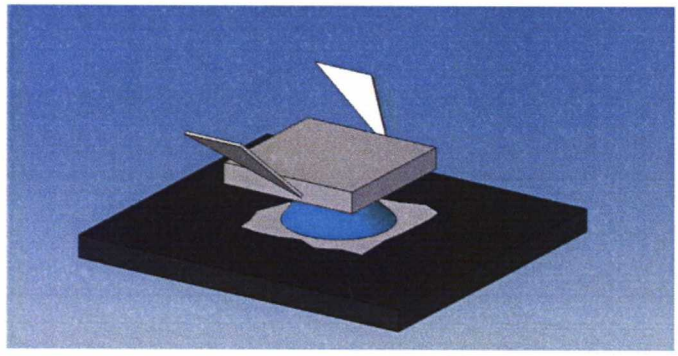

Figure 2: Illustration of self-alignment experiment on complex alignment pattern. A droplet of liquid is dispensed onto hydrophilic pattern on hydrophobic background, and the microchip is positioned on top of the droplet using microgripper. After the microchip is released, it will self-align with respect to the pattern.

In order to understand the phenomena which are present when microchips are aligned with complex patterns, the models for self-alignment process are created in this master's thesis. They are used to acquire understanding of the effect of each process parameter.

The objective of the study can be condensed into following research questions:

- What is the effect of pattern design on self-alignment on segmented four-pad pattern?
    - What is the effect of hydrophobic gap in the pattern?
    - What is maximal initial offset for successful alignment?
- How do the defects on the pattern edge alter the alignment position?
- How does the jaggedness of the edges affect alignment accuracy?
- How do material properties, hydrophobicity and hydrophilicity, affect the alignment reliability?

The rest of this master's thesis is arranged as follows: first the state-of-the-art microhandling techniques for microassembly are reviewed. Then capillary self-alignment and simple models for liquid/solid interactions are introduced. In the third section, modelling methods for capillary self-alignment are reviewed. The fourth section describes development of Surface Evolver model for self-alignment on segmented patterns, and presents the results of the model with comparison to published experimental results. In section 5, a simulator for chip trajectory during self-alignment is presented. Section 6 studies the accuracy of self-alignment on poorly defined patterns, both in theory and experiments. In section 7, self-alignment on tapered patterns is modelled and failure conditions are developed and compared with experimental observations. The results are concluded in section 8.

2 Microassembly and microhandling technologies

In this section, the state-of-the-art of microassembly and microhandling technologies is presented, and the basic principles of self-assembly and self-alignment are introduced.

During the past thirty years, microfabrication, microhandling and microassembly have been developed from simple bulk micromachining to the fabrication and assembly of various devices, such as ultrasound motors in cameras, acceleration sensors in mobile phones and small medical devices for point-of-care diagnostics, for example, measuring the level of blood glucose. These systems are called Micro-Electro-Mechanical Systems (MEMS), because they contain at least one microfabricated component, have electrical and mechanical functionality and are in general small in size.

Compared to conventional assembly on a macro scale, for instance cars, microassembly has several challenges that are not present in the macro world. They are related to the miniaturizing of the whole system. In order to accurately position a microchip with dimensions of 500 μm × 500 μm × 50 μm without large relative error, the requirement for robot's accuracy is significantly higher than if the size of the part is in the range of centimetres and metres. Another phenomenon related to miniaturizing is scaling effect.

The scaling effect describes the changes in quantities, such as speed, volume, and luminosity, when the *size* of the system changes. The most commonly known scaling law is that when length increases, the increase in area is quadratic and volume cubic. Due to the scaling law, gravitation becomes almost negligible in micro world, since it is related to the mass, and therefore to the volume of the object – and the volume decreases 1000 times when length decreases 10 times. Furthermore, as the size of the system decreases, the increase in effect of adhesion forces, such as Van der Waals forces and electrostatic attraction, is caused by the scaling effect. This is because they are related to the area of the object, which does not decrease as fast as the volume. Figure 3 shows an illustration of scaling of different forces. In figure 3 it can be seen that when the length scale is smaller than 1mm, capillary force clearly dominates the gravitation. [5]

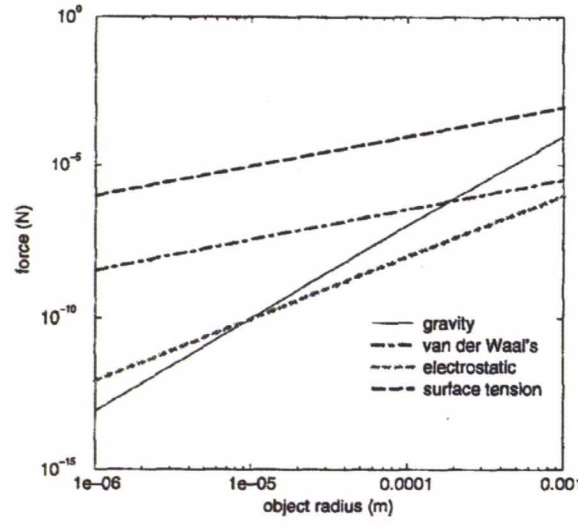

Figure 3: Effect of scaling laws to magnitudes of different forces. In length scales below 1 mm, surface tension force is dominant. [5]

The basic assembly task is to pick, transport and release a micropart to an assembly location, and then attach it there. Usual assembly tasks are e.g. placing a functional die onto the lead frame and bonding it, then wire-bonding the electrical contacts of the die with electrodes in the lead frame [6]. Usually microchips or dies are transported on sticky tape, and the picking force has to be strong enough to break the adhesion between the micropart and the tape. Sometimes the dies are pushed with a needle, thus decreasing the contact area between the part and the tape, which in turn decreases adhesion force and aids picking [7].

2.1 Robotic microhandling

The state-of-the-art in microhandling technologies is still a robotic pick-and-place machine. These machines have a microgripper which is able to pick up a micropart and then position it in a pre-defined location. Although the operation is serial, industrial machines can reach high speed of one pick-and-place cycle in less than 100 ms [8]. The challenges are that parts easily stick to the gripper, due to electrostatic attraction and other adhesive forces, which reduces the positioning accuracy. Another requirement is that the gripping mechanism should not damage the fragile micro components, such as electrically functional microchips.

Picking is usually solved by using a vacuum gripper [8]. Vacuum grippers work by creating a vacuum that sucks the part onto the gripper head [9]. The benefits of vacuum gripping are that the part is usually easy to detach by switching off the vacuum, and that handling is very gentle, leaving no residue, and it does not damage the parts. The drawbacks of vacuum gripping are that only certain shapes can be picked up. They should have a flat surface, or otherwise the gripper head should be specifically designed for the part, which in turn is not necessarily cost effective.

Another solution is to use micro tweezers. This approach is close to macro world solutions, where friction between the part and the gripper is used to pick the part up. Tweezers can be modified to handle the part even with six degrees of freedom (6-DOF) [10]. However, the control of micro tweezers is not as straightforward as that of vacuum gripper, since the system has more degrees of freedom.

In addition, the capillary force can also be exploited in gripping. A few capillary gripper designs have been proposed and modelled, and the principle of picking is to add a liquid droplet between the gripper and the part, so that surface tension force attaches the part to the gripper [7], [11]. The benefits of the capillary gripper are that its effectiveness increases when the size of the part is scaled down, and that it can be designed to self-align the part to the correct position and orientation automatically [7]. However, the capillary gripper may leave residue on the surface of the part, and liquids, especially water, are not compatible with all microcomponents.

There are other mechanisms that can be used for gripping or transporting, such as electrostatic grippers, snap-locking grippers, optical tweezers and vibration [8]. They are application specific, for example optical tweezers can be used for cell manipulation due to their gentle operation principle.

2.2 Self-assembly and hybrid assembly

Self-assembly processes in nature are both efficient and robust. Molecules, cells and whole organisms are assembled without external guidance, by the inner design of their

components. Similar approach to microassembly is very appealing, because the traditional microassembly techniques based on picking and placing become inefficient when the size of the microchips is reduced to few hundred micrometres [2], [12]. Therefore, self-assembly has been proposed to solve the trade-off problem between high accuracy and high throughput [3], [13].

In microassembly, self-assembly can be achieved with wide range of techniques, but the principle of the assembly is the same as in nature: the system is designed so that the correct position and orientation of the parts results in minimization of system's energy [8]. Self-assembly can be realized using shape matching, capillary forces or electric and magnetic properties of the parts, such as magnetic manipulation or dielectrophoresis [2].

Self-assembly approach has several advantages compared to robotic assembly. Firstly, the process is parallel, which means that the assembly parts can be fed in large batches and they assemble simultaneously. This increases the potential throughput of the system. Secondly, the assembly is more robust and accurate than robotic placement, because there is no adhesion between the tool and the part, and the accuracy of the robot does not limit the final accuracy. On the other hand, self-assembly is a stochastic process, and thus excess amount of parts are sometimes needed in order to achieve high throughput [2]. In addition, external agitation may be needed, so that the parts are able to get in contact with the assembly sites [2].

One example of self-assembly is surface tension driven self-alignment, or capillary self-alignment [13]. In capillary self-alignment, liquid surface tension is used for creating the force that aligns the micropart onto desired assembly site. More details about the capillary self-alignment process are given in section 2.3.

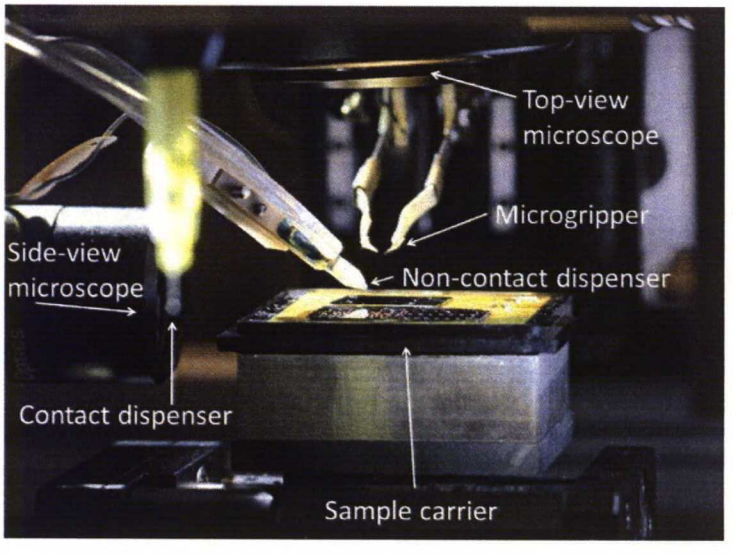

Figure 4: Hybrid assembly station with two microscopes, for top view and side view, microgripper, contact and non-contact dispensers and sample carrier. The 2-DOF (Degree Of Freedom) stage below the sample carrier allows moving the samples in lateral dimensions. The gripper can be moved vertically for picking and placing.

In hybrid assembly [4], robotic tools are combined with self-assembly in order to achieve the benefits from both approaches. The parallel and accurate self-assembly

process is integrated to serial robotic operation, resulting in increased performance. Chips are brought near the assembly site using a robotic handling tool and the final alignment is realized using e.g. surface tension driven self-alignment [8]. Hybrid assembly station with capillary self-alignment capability is shown in figure 4. The benefits of hybrid assembly, compared to capillary self-alignment alone, are that the part feeding is more deterministic, which ensures that the parts get into contact with their assembly sites [4]. In addition, the requirements for robot's accuracy can be relaxed and thus the speed of the robot can be increased.

2.3 Droplet assisted capillary self-alignment

Droplet assisted capillary self-alignment, which is referred simply as self-alignment further in this thesis, is based on energy minimization of the liquid droplet. Surface tension of the liquid is used to create a force which will move the microparts to the desired location.

The principle of capillary self-alignment is illustrated in figure 5. An alignment pattern is used to confine a liquid droplet to the assembly site. When a chip touches the droplet, a liquid meniscus is formed between the chip and the pattern, as in figure 5 b. The initial misalignment of the chip, i.e. the bias and twist (see figure 6), causes the liquid meniscus to stretch (figure 5b), which increases the potential energy of the system. When the chip is released and is free to move, the restoring force from the liquid meniscus draws the chip perfectly on the pattern (figure 5c). If volatile liquid is used, the droplet evaporates and the chip comes into contact with the target site (figure 5d). Non-volatile liquids may be used to e.g. glue chip onto the target site [13].

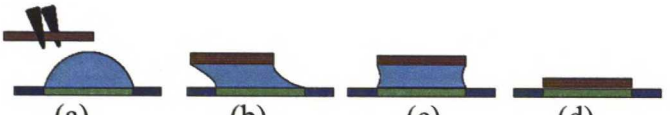

Figure 5: Principle of capillary self-alignment: (a) first droplet is confined to the target site with an alignment pattern, which is usually a high wettability pattern (green) on a low wettability surface (dark blue). (b) Then the chip is brought in contact with the droplet and the droplet wets the chip surface. (c) The chip self-aligns with respect to the pattern due to minimization of surface energy, and (d) finally the droplet evaporates and the chip is left in contact with the target site.

The alignment pattern is usually a hydrophilic area on a hydrophobic background [1], [14], but it can also be a height difference between two areas [15], [16]. Hydrophilic pattern on hydrophobic background can be achieved using Self-Assembled Monolayers (SAMs), which are one molecule thick layers which bind selectively to different surfaces, for example, to gold surfaces but not on silicon [13], [17]. The disadvantage of SAMs is that they wear off in time, so that the treatment should be done right before the self-alignment. Another possibility to increase hydrophilicity of certain area is to expose the area to oxygen plasma, which creates polar groups to the surface. Fluoropolymers are very hydrophobic, and therefore, for instance, aluminium patterns on Teflon background [1] can be used for self-alignment. Superhydrophobic surface can be achieved by coating a rough surface with fluoropolymer [18], which can be applied to self-alignment by patterning the silicon substrate with rough areas for hydrophobic

background and coating everything with fluoropolymer. Although the pattern itself is also hydrophobic, the self-alignment is still possible thanks to the superhydrophobic background [19].

If the assembly is done inside water, a hydrophobic area on hydrophilic background is used, and the droplet liquid is non-polar, meaning that it is not soluble in water, such as hexadecane [13]. This type of alignment is called fluidic self-alignment. The principles of self-alignment are, however, similar regardless of the surrounding media: self-alignment may be realized in water, air or some other liquid or gas [2].

The alignment accuracy in surface tension driven self-alignment is said to be as good as the manufacturing accuracy of the alignment pattern and the microchip [4]. Sub-micro metre accuracy [2] and high yield are achievable and the speed of one chip aligning is in the range of few tens or hundreds of milliseconds [4].

The list of terms related to self-alignment and their explanations is shown below.

- Bias: the translational misalignment, defined in figure 6.
- Twist: rotational misalignment of the chip
- Target site: The position where the chip should be assembled
- Substrate: The background material on which the target site is fabricated: area outside of the target site
- Pattern or self-alignment pattern: Chemical and/or topographic pattern that confines the liquid to the target site
- Pad: a part of more complex pattern, e.g. four hydrophilic square pads form the segmented alignment pattern. If the pattern is not segmented, pad refers to the full pattern
- Restoring force: The lateral force that aligns the chip, originates from the capillary force of the liquid meniscus.

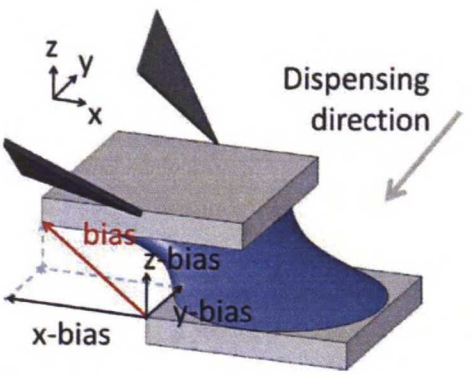

Figure 6: The definition of bias and coordinate system in hybrid assembly, figure from [4]. The z-bias is also called the height of the liquid meniscus.

2.3.1 Liquid droplet on solid surfaces

A droplet on a plane surface forms a contact angle with the solid surface, as shown in figure 7. When the droplet is at rest, the contact angle is unchanged and it is called static contact angle. If the droplet is sliding on a surface, the contact angles in advancing and receding fronts are different from each other: there is hysteresis and the angles are called advancing and receding contact angles, respectively. The edge of the droplet on surface is called three phase contact line (or simply contact line), because it separates

three phases: liquid in a droplet, the solid plane and the air that surrounds the droplet [20].

The contact angle is often taken as a measure for the wettability of the surface, which means that surface is regarded as hydrophilic when the contact angle with the water is less than 90°, and hydrophobic if the contact angle is over 90°. On hydrophilic surfaces, the droplets will spread more than on hydrophobic surfaces. If other liquid than water is used, high wettability surface is called lyophilic and low wettability surface lyophobic. The surface is superhydrophobic if the contact angle exceeds 150°.

The wettability of the surface depends on the surface energy of material in air (or surrounding liquid, if the system is immersed in liquid), as well as the interactions with the liquid and the surface. In general, higher surface energy of material decreases the contact angle and higher surface tension of liquid increases the contact angle. Surface tension and surface energy are related, so that they have same magnitude but different unit: unit of the surface tension and the surface energy are N/m and J/m^2 respectively. For example, surface tension of the water in air is 72,8 mN/m, and the surface energy is 72.8 mJ/m^2 for water-air interface.

The relation between contact angle θ and surface energies and surface tension is Young's equation [20]

$$\gamma_{sa} - \gamma_{sl} = \gamma_{la}\cos\theta \tag{1}$$

where γ_{la} is the surface tension of the liquid and γ_{sa} and γ_{sl} are the surface energies of solid/air and solid/liquid interfaces respectively. Young's equation can easily be understood when force balance at three phase contact line is illustrated as in figure 7.

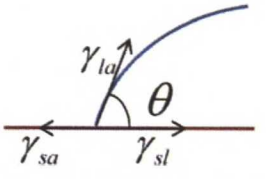

Figure 7: Formation of contact angle when droplet rests on planar surface. Force balance at three phase contact line defines the contact angle.

If the surface underneath the droplet is heterogeneous and contains e.g. stripes of hydrophilic and -phobic areas, the contact line shape deviates from a circle. In other words the hydrophilic/phobic patterns confine the droplet onto hydrophilic area [21]. The confinement of the liquid to the target site is the most important step in designing the self-alignment assembly process, since liquid overflow from the pattern is known to cause misalignment [14], [22]. This means that the wetting contrast between hydrophilic pad and hydrophobic background must be large enough [22].

Another way to confine liquid is to use solid edge [15]. The liquid is not able to overcome the sharp height step, unless the contact angle on the pattern edge exceeds a certain maximum. The maximum contact angle θ at the edge is modelled with Gibb's inequality [23]

$$\theta_0 \le \theta \le (180° - \varphi) + \theta_0 \tag{2}$$

where φ is the angle of the edge and θ_0 is the advancing contact angle on the surface.

3 Modelling methods for capillary self-assembly

Self-alignment is a physical process, where the surface tension of the liquid is used to bring the microchips onto target site. At its best, self-alignment is very accurate, fast and reliable. Different modelling methods for self-alignment have been developed, and they help understand the effect of process parameters, such as volume of droplet and initial misalignment. However, these methods differ from each other in complexity and applicability. In this section, the currently most used methods are described and compared with each other.

Modelling the phenomena containing liquid droplets and solid parts includes many challenges. Firstly the interaction between the liquids and solids should somehow be addressed, and the effect of non-rigid shape of the liquid/air interface should be captured in the model. In practice, there exist three different modelling methods: simplified geometry based models, numerical modelling and dynamical modelling. In geometry based methods [22], [24–27], liquid shape is approximated with simple analytical shapes and the energy of the system is calculated from surface energies. Numerical modelling, e.g. [22], [28], captures the curvature shape of the liquid with finite element method. Dynamical models [29–31] take into account the velocity profiles inside the liquid droplet, as well as the viscosity of the liquid and damping of the motion.

Theoretically self-alignment is based on principle of minimum energy: the system moves towards the configuration which minimizes the free energy of the system. In capillary self-alignment, the system's free energy is the sum of all surface energies in the system. Thus the system's energy is minimized by minimizing the surface area of the droplet and minimizing the high energy interfaces, e.g. reducing area between water and hydrophobic surface.

One way to look at the problem is that the liquid meniscus can be regarded as a spring. When the chip is biased, energy is stored to the meniscus, and this energy is dissipated when the chip self-aligns to the pattern. The energy is stored in the surface energy of the liquid, which increases when the area of the liquid-air interface increases [24]. The following methods are used to approximate the energy at different biases in order to reveal the "spring force" and the equilibrium position, i.e. the minimum energy position.

3.1 Analytical geometry based approaches

Analytical models of the self-alignment are approximations where the liquid curvature is neglected or liquid layer is assumed to be very thin so that height of the liquid can be neglected. Then the free surface energy of the system is calculated from

$$E = \sum \gamma_i A_i \tag{3}$$

where A_i is the area of each interface and γ_i is the surface tension at that interface [32].

3.1.1 Analytical model of liquid meniscus shape

The total free energy of the system, a kind of potential energy, is a function of bias and twist of the chip. The restoring force that aligns the chip is the gradient of potential

energy. Potential energy is linked to the surface area with surface tension, and surface area can be calculated when the shape of the liquid is known.

Simple analytical model for droplet shape is cylinder or parallelepiped, as shown in figure 8. The liquid curvature is neglected and the surface area of the liquid can be written for circular pads as in [24], [26] (figure 8b) and for square pad

$$E(x) = \gamma A(x) = 2\gamma L\sqrt{x^2 + h^2} \tag{4}$$

Where γ is the surface tension of the liquid, A the area of liquid-air surface, x is the bias in x axis, L is the length of edge of the pattern and h is the height of the liquid meniscus [22]. The equations for energy on circular and square pad correspond to each other when the perimeters of the pads are equal.

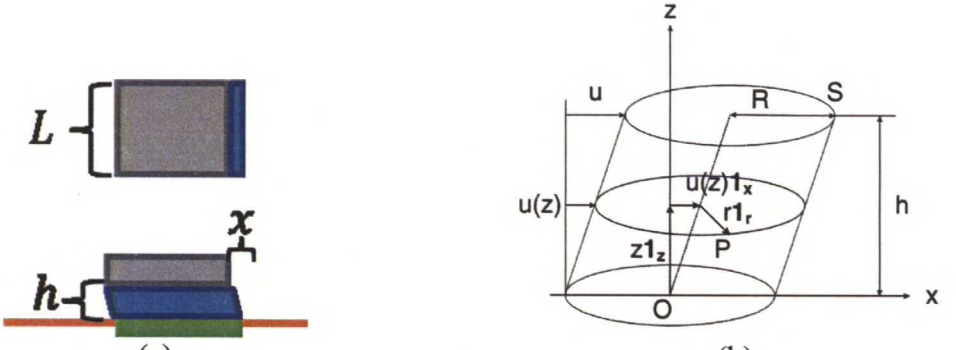

(a) (b)

Figure 8: (a) Definition of bias x, pattern and chip edge length L and height of the liquid meniscus h in parallelepiped approximation of the liquid shape. (b) Cylindrical approximation of liquid shape [26].

When the part is biased, restoring force $\vec{F}$ can be calculated by

$$\vec{F} = -\nabla E = -\gamma \nabla A \tag{5}$$

Eq. (5) holds with the assumption that only the liquid-air interface affects the energy and the other surfaces, e.g. liquid-chip surface, do not contribute to the restoring force, because their surface energy and area are constant.

Using (3), (4) and (5), the restoring force for square pattern is then

$$F = -2\gamma L \frac{x}{\sqrt{x^2 + h^2}} \tag{6}$$

Equation (6) shows that when the bias is much larger than the height of the liquid meniscus, restoring force is linearly related to the surface tension of the liquid and length of the pattern edge, which is parallel to the sift. The analytically calculated stiffness for circular pads is compared with numerical and experimental values in figure 9, showing that both numerical and analytical models overestimate the meniscus stiffness [26].

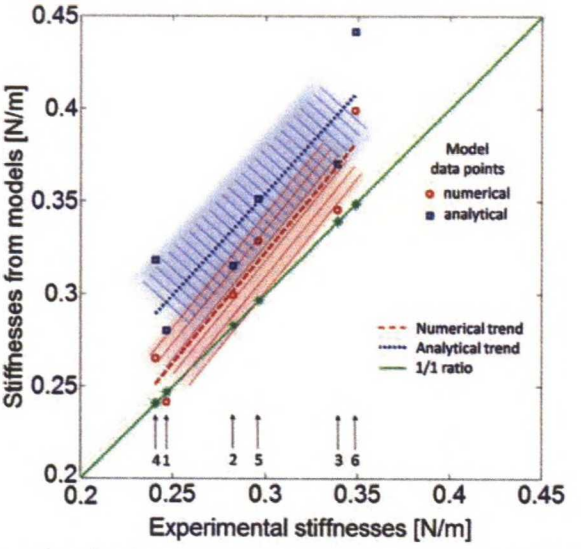

Figure 9: The stiffness of cylindrical liquid meniscus calculated with analytical model and numerical model (Surface Evolver program), compared to experimental results [26].

The twist of the chip has also been modelled similarly in [22], [27], but simple models compare well with experiments and numerical results only with twists less than 10°. Better agreement with experimental twist is achieved with numerical methods, presented in section 3.2.1.

3.1.2 Overlapping area between chip and the pattern

Overlapping models are relatively simple and they allow studying the alignment of complex shapes. They have been developed mainly for fluidic self-assembly, but apply also at least qualitatively to self-alignment in air. In fluidic self-assembly the assembly happens inside a liquid – normally water – and hydrophobic parts attach to hydrophobic target sites, with some low-polarity fluid in between. Therefore the liquid film is very thin, so that height of the liquid can be neglected. The fluid acts as lubricant and creates the self-aligning force. [25]

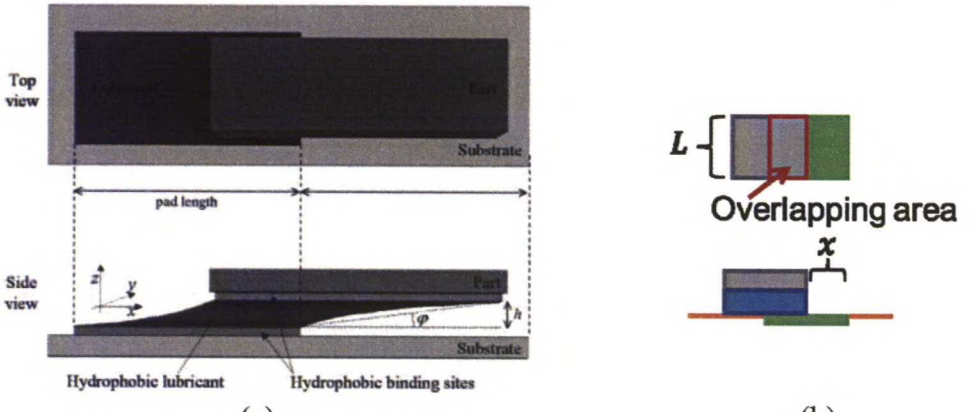

(a) (b)

Figure 10: Illustration of the overlapping area between chip and the pattern when the chip is biased (a) the liquid meniscus wets the chip and the pad completely [32] (b) the liquid wets the chip and the position of the chip defines the potential energy.

The model is based on the fact that alignment will try to maximize the overlapping area of two hydrophilic shapes (when water droplet is used in air) or two hydrophobic shapes (when lubricant droplet is used in water). This is intuitive, since maximizing overlapping area minimizes the high-energy surfaces between hydrophobic area and water and maximizes the low-energy surfaces between hydrophilic area and water. The energy of the system is related to the overlapping area, which is shown in figure 10, and therefore the energy landscape may be calculated using 2D convolution of the pattern and the chip [25]. For example, energy landscape for complex C-shaped pattern is illustrated in figure 11.

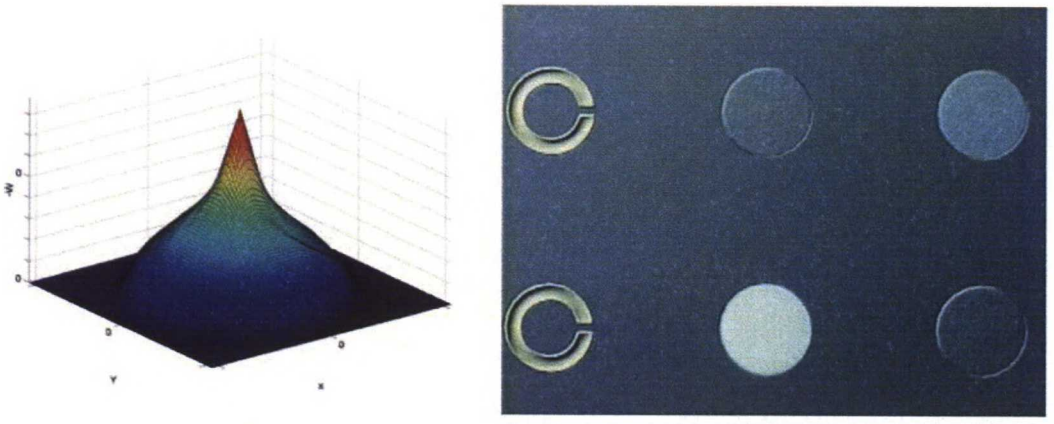

(a) (b)

Figure 11: (a) The surface energy of the system with different x and y bias for complex C-shaped patterns. (b) Alignment patterns with C-shape and aligned chips. [25]

The derivation of the model assumes that, as in figure 10a, the lubricant layer between pad and the chip is so thin than the lubricant interface with surrounding medium (water) is just the area of the meniscus projected to the substrate plane. Then the restoring force for positive bias is

$$F=-2\gamma_{LM}L \tag{7}$$

Where γ_{LM} is the surface tension of lubricant-medium interface and L is the length of the pad edge [32], [33]. This is similar to the force from (6) when the bias is much larger than the height of the liquid meniscus.

Another way to use similar approach is approximate the free energy of the system as in figure 10b, so that the shape of the liquid meniscus is unchanged during the alignment [1]. Then the energy of the system is approximately

$$E=\gamma_p A_{ol}+\gamma_s(A_c-A_{ol}) \tag{8}$$

where γ_p and γ_s are the surface energies of liquid-pad and liquid-substrate interfaces, which also take into account solid-air interface energy: they can be calculated using (1), e.g. $\gamma_p=\gamma_{la}\cos\theta_p$. A_c is the area of the chip and A_{ol} is the overlapping area of the chip and hydrophilic parts of the pattern. Since chip area is constant, it does not contribute to

the restoring force and can be left out. The energy that is minimized during alignment, is then

$$E = (\gamma_p - \gamma_s) A_{ol} \tag{9}$$

When background is more hydrophobic than the pattern $\gamma_p < \gamma_s$, the minimum energy is reached when the overlapping area is largest [1]. This method assumes that the liquid may wet also the background but the wetting contrast finally brings the liquid and the chip onto target site.

With overlapping method it is possible to derive potential energy landscapes for different chip/target site shapes and design patterns that provide orientation specific alignment [34]. Method can also be used for predicting the alignment position for different alignment pattern shapes and estimating the restoring force.

However, the overlapping model becomes inaccurate when liquid volume increases so that liquid curvature becomes significant or bias is smaller than the liquid thickness. In addition, it is not possible to predict the final position of the chip if energy landscape has local minima or flat parts. This is because they induce ambiguity in position, and therefore dynamic factors, such as the velocity of the chip, affect the final position.

3.2 Numerical models

Finite Element Methods (FEM) can be used for simulating the behaviour of complex shapes and multiple physical loads, e.g. tensions, gravity etc. FEM models consist of meshed object that represents the physical system. In modelling of capillary self-alignment, liquid is typically represented with mesh, as shown in figure 12a. In [14] the total restoring force is calculated by summing the restoring forces from virtual surfaces, so that even complex shapes can be analysed (figure 12b). However, in this model, the liquid curvature is still not taken into account.

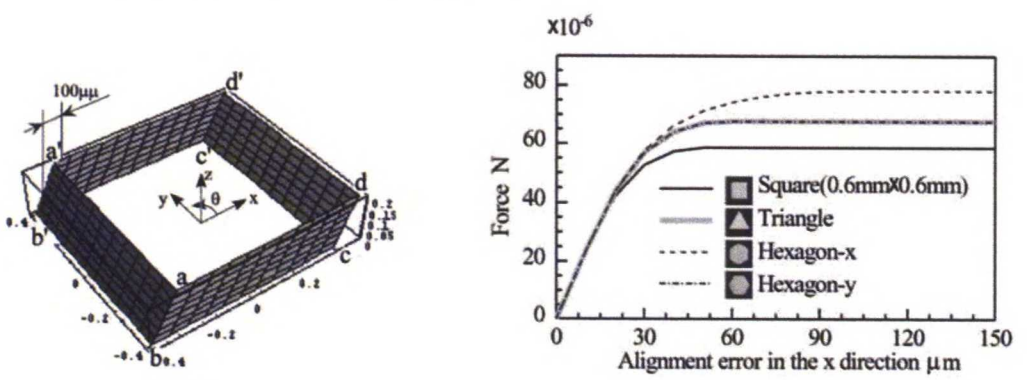

(a) (b)

Figure 12: (a) Virtual surfaces that are used to describe the liquid meniscus and (b) the restoring force calculated for different pattern shapes, from [14].

To take into account the liquid curvature, the FEM simulation that resolves the real shape of the liquid meniscus is often needed. The restoring force can then be derived from adding a small displacement to the chip position and calculating resulting energy difference [35].

Numerical methods that take into account wetting properties and the shape of the liquid meniscus, as well as other geometrical constraints, can be used to model also one

failure mode of self-alignment, the overflow of the liquid. In [14] the volume that causes overflow was calculated by comparing the theoretical restoring force to the confinement capability of the pattern. However, the overflow was observed frequently even with droplet volumes that were smaller than found in theory.

3.2.1 Surface Evolver program

One widely used numerical program is Surface Evolver [28], which can be used to simulate liquid interfaces, soap films and complex geometries. The energy and restoring force during self-alignment can be simulated with Surface Evolver, as shown in figure 13, which represents different misplacements of the chip. In this section, the basic principles of Surface Evolver are explained.

In Surface Evolver, the liquid is represented as mesh that consists of vertices and connecting edges, so that surface is divided into triangles. The program starts with very sparse mesh and refines it to form a better representation of the liquid interface, as shown in figure 14.

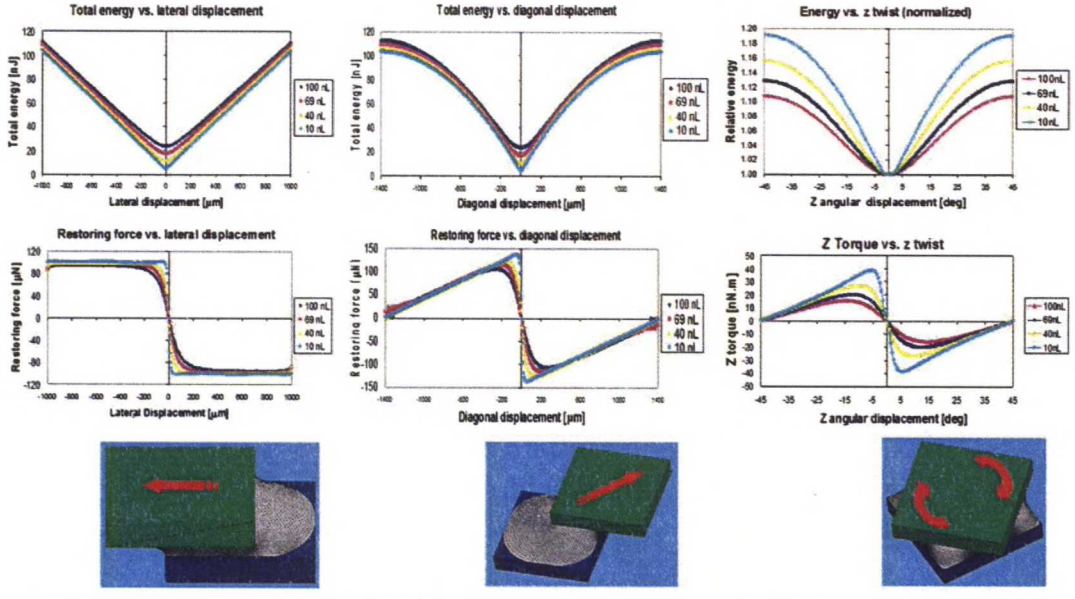

Figure 13: Energy and restoring force during different misplacements of the chip, simulated with numerical program Surface Evolver [2].

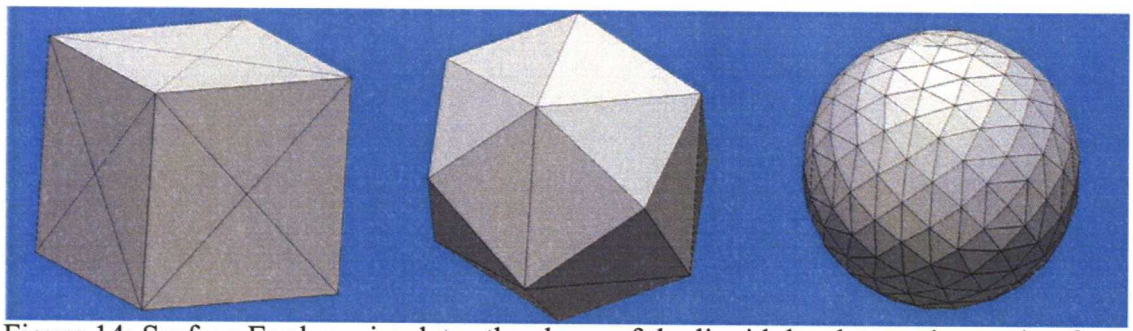

Figure 14: Surface Evolver simulates the shape of the liquid droplet on air, starting from sparse mesh and evolving towards minimum energy shape with smallest surface area, preserving the volume of the droplet.

At each step of evolving, the program calculates the force acting on each vertex using gradient descent method. Then each vertex is moved along the energy gradient at pre-defined step that is also related to the magnitude of calculated force. During the evolving, some triangles in the mesh may become stretched so that they are far from equiangular. This may cause problems in moving the vertices and thus the mesh can be re-triangulated to get more uniform triangles.

The boundary conditions for liquid, such as contact angles with solid planes or geometric shapes that confine the liquid, are introduced using boundaries and constraints for the movement of vertices. For example, the vertices that lie on the solid surface can not sink through the surface, and they have extra energy associated to them, which represents the forces acting on the contact line. In so doing it is possible to define different wetting properties for solid surfaces. To reduce the computational load and problems with vertex movements on constraints, the vertices that lie on solid surfaces are usually replaced with integral over the contact line. The idea in replacing the vertices of the liquid with path integral is that, in reality, only the contact line is critical for defining the liquid shape, because in liquid/solid interface the liquid follows the profile of the solid. The shape of the contact line depends on the surface energy of the area in liquid/solid interface, which lies within the contact line. Therefore the surface energy can be represented with path integral around the contact line.

The energy is calculated by integrating the surface energies of each triangle and accounting the extra energies from boundary conditions. In addition to that, physical loads, such as pressure or gravitation can be taken into account.

Surface Evolver can be used to model complex shapes, such as hydrophilic/phobic stripes [36]. Therefore it's not surprising that is widely used for its capability to tackle complicated three dimensional processes: recent studies have investigated e.g. wetting of the target site [16] and restoring forces in self-alignment [26], [37–39]. However, writing the boundary conditions for energy on complicated shapes is difficult and requires knowledge of advanced calculus. In addition, the gradient descent method for moving the vertices can encounter troubles at sharp wettability boundaries [36]. In [26] it is shown that compared to experimental restoring force, Surface Evolver overestimates the force and stiffness of the liquid meniscus, which is seen in figure 8.

3.3 Dynamical models

Dynamical models has been proposed for studying the time constants [31], effect of viscose, low-surface tension liquids [29] and the oscillating behaviour of the alignment [24]. Dynamical models have been derived only for simple geometry of axially symmetric liquid meniscus with circular pad and chip. The dynamical behaviour of self-alignment system is modelled with second order dynamics [24], [29–31], as shown in figure 15. The system is then

$$m\ddot{x} = -k(x)x - c\dot{x} \tag{10}$$

where m is the mass of the chip, k is the stiffness of the liquid meniscus in lateral direction and c represents the viscous force from the viscous stress inside the liquid [31]. Usually after that a linear velocity profile inside the droplet is assumed and the viscose shear force is calculated either using Newton's law for viscous fluid [29] or Navier Stokes equation [30], [31]. In [30] also non-linear velocity profile has been studied, as well as the coupling of the parameters. The spring constant k is usually calculated with Surface Evolver or analytical model as in section 3.1.1 [30], [31].

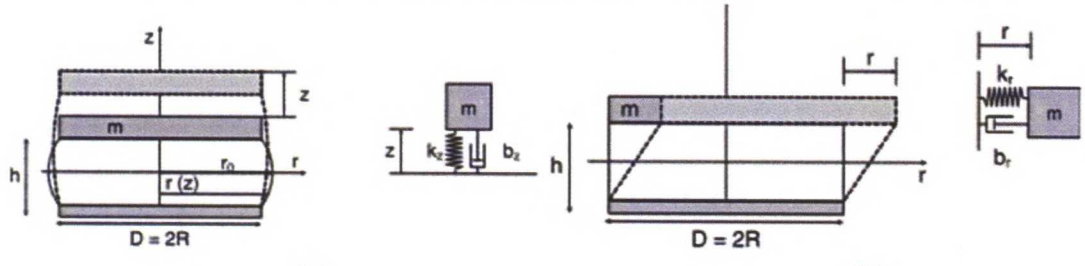

Figure 15: The models for vertical (a) and lateral (b) movement of the chip, figure from [31]. Liquid meniscus is modelled as second order system with viscous damper. [24], [29]

The main challenge with dynamical models is the coupling of the parameters: in [30] it was shown that the characteristic time scales of the chip motion and the flow inside the liquid are so similar that the velocity inside the liquid and the chip velocity are strongly coupled. This means that the damping of the system depends not only on the velocity of the chip but also on the velocity of the liquid. The coupled dynamic modelling method in [30], run in fluid dynamics software, showed that the damping force is much larger than in uncoupled dynamical models. However, the simulation is computationally very demanding.

Lambert et al. [31] used spectral analysis to solve the coupling problem in ordinary differential equations. Their results are close to Lu and Bailey's work [30], but the method reduced computation time. They also provide a map for damping times with respect to non-dimensional parameters representing diffusion coefficient and mass ratio.

Comparison to experiments show that dynamical models compare well with high viscosity fluids, where damping time is small [29], [31], whereas with low-viscosity fluids, e.g. water, and under damped systems the agreement with experiments is not as good [24], [31].

3.4 Summary of modelling methods for capillary self-alignment

The most used models for capillary self-alignment in microassembly are analytical, geometry and energy based methods or numerical FEM models, where liquid presented with mesh, e.g. using Surface Evolver program. Dynamical models have been developed, but they are computationally demanding and do not allow the analysis of complex pattern and chip shapes or wetting properties of the pattern, background and the chip.

The most efficient method when designing the alignment pattern shape is probably to analyse overlapping area, because it can be done either analytically or numerically relatively easily and fast. When the wetting properties of the materials have large effect, Surface Evolver can be used to see, how the wetting of the pattern will affect the alignment. Table 1 summarizes the practical properties of the most common modelling methods and compares their benefits and restrictions.

The modelling methods described in this section provide tools for analysing the effect of chip and pattern shape and size to the self-alignment. They are, however, mostly limited by their static or quasi-static assumptions, so that the evaporation of the liquid or the liquid spreading to initially non-wetted areas is not taken into account. In addition, the most common failure mode – overflow – is usually excluded from models and the liquid is assumed to stay perfectly inside the pattern. Surface Evolver can be used to model overflow, but complex patterns with different wettability are difficult to model and may lead to numerical problems. There has been suggestion to improve this by updating the mesh separately for the vertices on wettability boundaries [36].

Other dynamical factors, such as the evaporation of volatile liquid or initial energy of the chip when it touches the liquid, could be taken into account to further improve the results of current models. Current models provide useful guidelines for self-alignment process design, but experimental tests are still needed to verify the modelling results.

The goal of modelling in this thesis is to reveal, what happens when the alignment pattern has complex shape, such as segmented structure or jagged edges. Because wetting of the pattern is known to have effect on self-alignment reliability [40], the model needs to be able to capture the effect of wetting. Therefore Surface Evolver is chosen as primary modelling method for this study. Another possibility to model the alignment on complex patterns is overlapping area analysis, which is used as supplementary tool.

Table 1: Comparison of the presented modelling methods

	Validity area	Results	Geometries that can be modelled	Benefits	Restrictions
Dynamical	High viscosity fluids	Damping time, trajectory of the chip	Circular pads	Alignment time and trajectory of the chip is approximated	Computationally demanding Current models do not include evaporation
Numerical, Surface Evolver	Sufficient amount of liquid to avoid numerical problems	Surface energy of the system, restoring force to different directions	Complex wetting patterns, 3D shapes	Droplet shape taken into account Contact angles are taken into account → simulates the wetting Gravity can be included	Complex patterns are difficult to model Convergence of the liquid Quasi-static model
Analytical, parallelepiped	Liquid does not overflow to the substrate	Analytical form for surface energy → restoring force	Circular, square or rectangular	Simple Valid also near the bias = 0.	Wetting behaviour not taken into account
Overlapping area	Height of the liquid meniscus << bias	Energy landscape with different biases / rotations	Complex shapes	Simple Easy Qualitative analysis of the suitability of pattern geometry to self-alignment	Applies only for very small volumes of droplet; not usually the case with self-assembly in air

4 Self-alignment on four-pad pattern

In typical assembly task, a microchip should be placed onto substrate with accuracy so that the electric contacts can be formed between the chip and the base. Contacts can be achieved using wire bonding, where the contacts on the chip are connected to the contacts aside the chip by metal wire [6]. The contacts may also be underneath the chip, which means that the solder bumps on the chip will be located onto contacts and create electric connection when melted. This is called flip-chip packaging [6]. Flip-chip packaging simplifies the assembly process and may also create more reliable package, since breaking or delamination of wire bond is common failure mode [6]. For flip chip alignment, the chips need to be placed so that the misalignment is smaller than the size of one bump [41]. This is limiting the capability of the process.

In low-pin count chips, e.g. LED or RFID chips, there are only from two to four contacts, as shown in figure 16. If flip-chip method is used, it would be convenient to use the electric contacts as a reference for self-alignment, so that same lithography mask could be used for contacts and defining alignment pattern. Therefore in this study, a segmented four-pad pattern is chosen to represent contact pads on RFID antenna, and the goal is to model the self-alignment on this kind of pattern. Parts of the work in this section are published in [1].

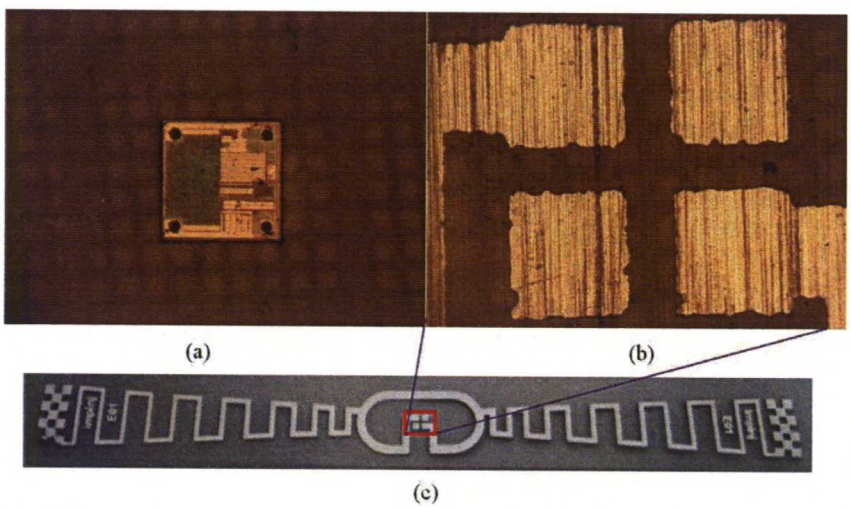

Figure 16: RFID die and the antenna pattern where the die should be aligned. From [1].

To understand the self-alignment of RFID dies on the four-pad patterns with water droplet, the influences of the key parameters that may affect the self-alignment process should be understood. They are e.g. the volume of the droplet, the gaps between the pads, the speed of the self-alignment and the initial bias. Typical alignment test is shown in figure 17. Although previous studies have reported the effect of size [15], [42] and shape [13], [14], [34] of the target site, the initial bias [4], the volume of the liquid droplet [4], [14], [15] or the choice of the liquid [31], [42] those studies are for rectangular or specially defined patterns and cannot provide a direct answer to our questions.

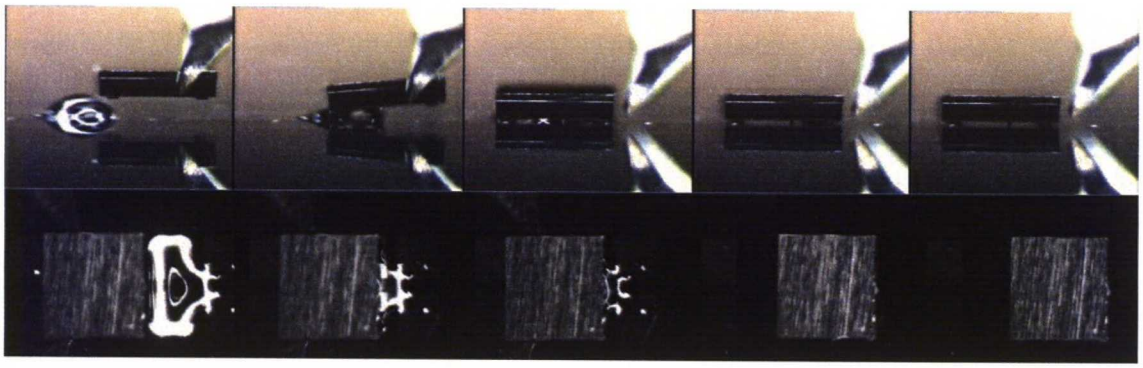

Figure 17: Side view and top view of self-alignment experiment on four-pad pattern. From [1]

As shown in previous section, suitable modelling methods for patterns with complex shape are numerical methods and overlapping area analysis. Because segmented pattern clearly affects the shape of the liquid droplet, as seen in figure 18, Surface Evolver is used for simulation in order to capture the shape of the droplet. As presented before, Surface Evolver finds the (quasi) static equilibrium for liquid medium by evolving surface using gradient descent method.

Figure 18: Wetting on segmented pattern. The shape of the droplet is affected by hydrophobic gap between pattern segments, i.e. pads.

The model includes three elements, a die, a droplet of liquid and a pattern consisting of four hydrophilic pads on hydrophobic surface with spacing (gap) between the pads. Illustration of the pattern is shown in figure 19. The sizes of the patterns, including both the pads and the gaps, are 730 μm × 730 μm and 710 μm × 710 μm. The results, however, can be generalized to other pattern sizes using the non-dimensional analysis discussed in section 4.2. Since gravity is not considered in the simulation, the results are applicable only at the scale smaller than capillary length, which is 2.7 mm for water. Even though the results, as they are developed for specific geometry, are not directly extendable to other geometries, they can serve as the basis for cases that use the four segmented patterns as the building block.

In this study, the size of the pattern is also used for referring to the length of one edge of the square pattern, e.g. 730 μm. When the effect of parameters other than contact angles, such as the size of the gap, is studied, the contact angles with different parts of the pattern are fixed according to the properties of fabricated test pattern [1]: contact angles are 30° and 60° with pads and the substrate respectively. The axes for

describing the initial bias of the chip are defined as shown in figure 19, as well as the definition of the area of the pattern.

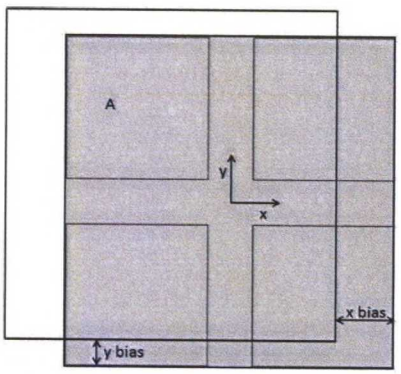

Figure 19: Definition of the axes: the chip is biased at negative x and positive y direction. Origin lies at the center of the four-pad pattern. Area A of the pattern is marked with grey.

4.1 Creating Surface Evolver model

Elements in created Surface Evolver model are the chip, liquid droplet and planar surface, where hydrophilic/hydrophobic pattern is defined. When wetting of the pattern is simulated in next section, there's no chip in the model, just the liquid droplet and the hydrophilic/hydrophobic pattern. The vertices on the hydrophilic/hydrophobic pattern are constrained so that they have to stay in contact with that surface, because otherwise the liquid might sink underneath the pattern or start floating, since gravitation is not taken into account.

As discussed in section 3.2.1, in order to define the contact angle for the liquid on the surface, Surface Evolver uses virtual surface energy, which is associated with each vertex lying on the surface. Simply put, the question in defining the hydrophilic/hydrophobic pattern is just how to define a sort of cumulative distribution function for surface energy. The surface energy on hydrophilic/hydrophobic pattern is

$$E(x,y) = \begin{cases} \gamma_{philic}, & \text{when on hydrophilic pad} \\ \gamma_{phobic}, & \text{when on background} \end{cases} \tag{11}$$

where γ_{philic} can be calculated from hydrophilic contact angle θ_{philic} using Young's equation (1) $\gamma_{philic} = -\gamma_{la}\cos\theta_{philic}$, and respectively γ_{phobic} from hydrophobic contact angle. When the energy is defined in this way, the forces acting on the vertices are in equilibrium when liquid contact angle is the correct contact angle, and thus the contact line movement ceases.

The cumulative distribution function is called energy content $\vec{w}$, and it is associated with each vertex on the contact line. The condition for using Green's Theorem is that $\vec{w}$ must be chosen so that $1°\ \vec{w} = M(x,y)\vec{\imath} + N(x,y)\vec{\jmath}$ and $2°\ \frac{\partial N}{\partial x} - \frac{\partial M}{\partial y} = E(x,y)$, where $E(x,y)$ is as defined above.

Then the energy from liquid/solid interface can be calculated using Green's Theorem:

$$\iint_S E(x,y)dxdy = \int_{\partial S} \vec{w} \cdot \vec{dl} \approx \sum_{vertices} |\vec{w}||\overrightarrow{\Delta l}| \cos(\sphericalangle \vec{w}, \overrightarrow{\Delta l}) \tag{12}$$

Where S is the liquid/solid interface, ∂S is the boundary or the liquid/solid interface and $\overrightarrow{\Delta l}$ is the vector from one vertex to the next one.

In search of suitable energy content $\vec{w}$, it all comes down to finding $M(x,y)$ and $N(x,y)$ so that second condition is met. Simple case is when the surface has hydrophilic stripe on hydrophobic surface, as shown in figure 20a. Then we can assume that $M(x,y)=0$, and the problem reduces to finding $N(x,y)$ so that $\frac{dN(x,y)}{dx} = E(x,y)$. From this we see, that the slope of the function in x direction should be equivalent to the surface energy. Thus $N(x,y)$ is a plane, where the slope in y direction is always 0 and slope in x direction is γ_{philic} when point (x,y) is on hydrophilic stripe, and γ_{phobic} when the point is on hydrophobic background. However, the functions M and N must also be continuous. Therefore the function N looks like in figure 16b. The result can also be obtained simply by integrating $E(x,y)$ with respect to x, but the explained approach helps to understand, how more complicated pattern shape is modelled. More detailed information about advanced calculus used in Surface Evolver can be found in Surface Evolver manual [43].

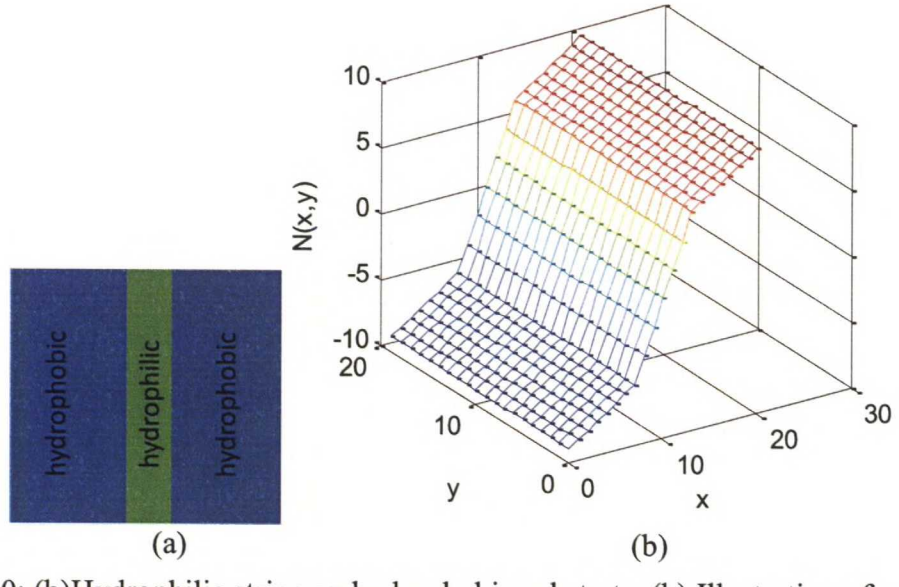

(a) (b)

Figure 20: (b)Hydrophilic stripe on hydrophobic substrate. (b) Illustration of energy content in Surface Evolver to define hydrophilic stripe on hydrophobic substrate.

In order to model four-pad pattern, we should keep in mind similar approach as previously, trying to find a function that has two different slopes, depending on the contact angle at the point (x,y). However, if we define the energy content $\vec{w}$ similarly as with hydrophilic stripe, the result is not continuous on the edges of the pads, which are parallel to x axis. In order to avoid this, coordinate axes are rotated 45° counter

clockwise, as shown in figure 21a. Now similar approach can be used, so that $M(\tilde{x},\tilde{y}) = 0$ and $\vec{w}(x,y) = \vec{w}(\tilde{x},\tilde{y})\vec{e}$, where $\vec{e} = \frac{1}{\sqrt{2}}(\vec{\imath} - \vec{\jmath})$. The mapping from new coordinates to original coordinates (x,y) is then

$$\begin{bmatrix} x \\ y \end{bmatrix} = \begin{bmatrix} \frac{1}{\sqrt{2}} & -\frac{1}{\sqrt{2}} \\ \frac{1}{\sqrt{2}} & \frac{1}{\sqrt{2}} \end{bmatrix} \begin{bmatrix} \tilde{x} \\ \tilde{y} \end{bmatrix}. \tag{13}$$

When $N(\tilde{x},\tilde{y})$ has been found, transformation (13) is used to return to original coordinates in x and y axis and solve energy content $\vec{w} = M(x,y)\vec{\imath} + N(x,y)\vec{\jmath}$. For four-pad pattern, component $N(x,y)$ of energy content is illustrated in figure 21b. Then, when the path integral of energy content over contact line is calculated, as illustrated in figure 20 a, the result is energy of the liquid/solid interface within the contact line.

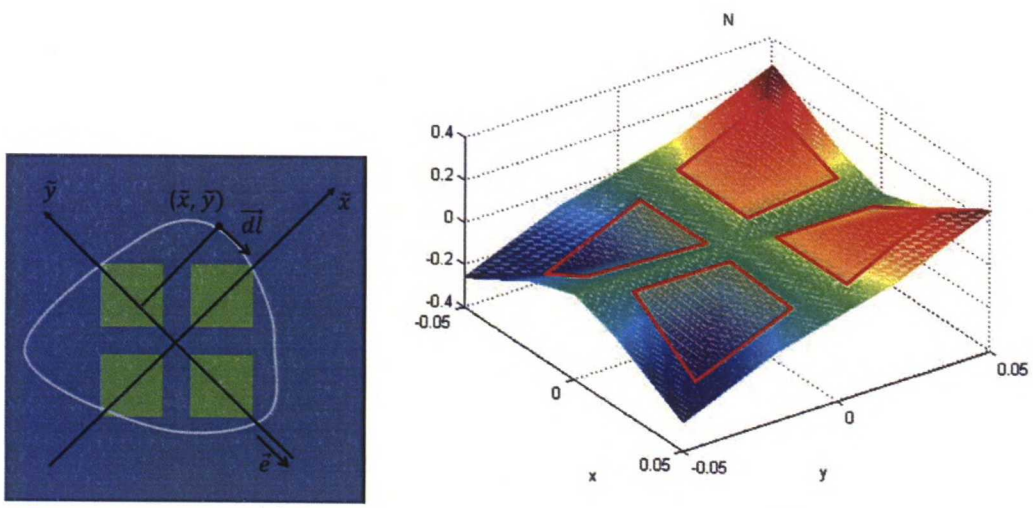

(a) (b)

Figure 21: (a) Illustration of hydrophilic four-pad pattern on hydrophobic background, light line shows the position of contact line, $\vec{dl}$ defines the orientation of the path integral and $\vec{e}$ is unit vector so that $\vec{w}(x,y) = \vec{w}(\tilde{x},\tilde{y})\vec{e}$. (b) The energy content visualized in MATLAB, the positions of the pads are highlighted with read polygons.

Surface Evolver does not support variables or functions in energy content definitions. [43]. Therefore macros are often needed when defining more complicated constraints and variables. In order to be able to loop through varying parameter values, such as the bias and gap size, and for visualizing the results, the Surface Evolver model is run by a MATLAB script. The parameter ranges are defined in the script, which creates corresponding energy content and writes it into a macro, which is then saved in a text file. The text file is added to the Surface Evolver data file during the execution of the code.

4.2 Wetting on four-pad pattern

Poor wetting of the target site is known as a common reason for failed self-alignment [14], [16], [44]. The importance of wetting and droplet volume is illustrated in figure 22. Poor wetting is the condition that the surfaces are only partially covered by the

water droplets, leaving unwetted surfaces. The volume of the droplet is one of the key parameters that affect the wetting of the target site. In case of a segmented target site, it is important that all the pads are wetted to avoid possible failure due to dry contact. When the chip is placed on the droplet, the capillary effect will aid liquid spreading onto those pads that it already has contact with. However, in experiments it was found that if the liquid has no contact to one pad, it will not spread to that pad even when the chip is added [1]. Therefore it is important to find out how to achieve good wetting in the case of segmented pattern. On the other hand, too large volume may also result in failed alignment due to overflow, as in figure 22c or decreased restoring force [15].

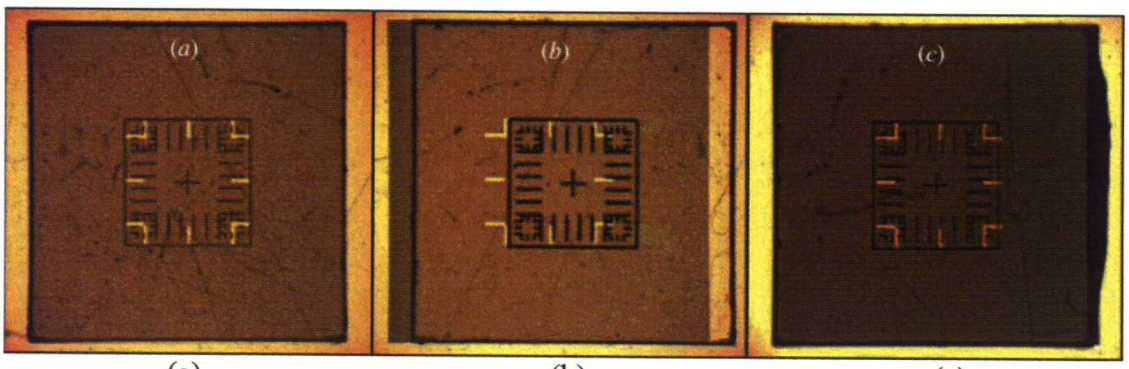

Figure 22: Success of alignment with different droplet volumes. (a) suitable amount of liquid results in good wetting and good alignment accuracy. (b) Too little amount of liquid causes alignment to fail. (c) Overflow of too large droplet damages the alignment. Figure from [45]

In this section the minimum volume for good wetting is found by estimating the energy for different droplet configurations, e.g. two different size droplets on different pads or one droplet wetting all the pads. When the droplet that wets all the pads has lowest energy of all other configurations, the amount of liquid will be sufficient for alignment. On the other hand it is important not to use excess amount of water in order to prevent overflow, as shown in figure 22c. The critical volume is defined as the minimum volume when the droplet wets all the pads, and it depends on the pattern configuration, namely the size of the pattern and the gap, and the wetting properties of pads and the substrate.

To find out the critical volume for different pattern configurations and wetting properties, the minimum energies of two cases are studied. In the first case, the droplet stays at the centre of the pattern, as illustrated in figure 23a. In the second case, the droplet either slips onto one of the pads (figure 23b) or is split onto two or more pads so that the volume of the droplets on each pad may differ. To find the minimum energy for the latter case, the number of droplets and their volumes are optimized with respect to the total energy of the system. The energy of one droplet on one pad is simulated with different volumes and the results are used as a look-up table for optimization task. To overcome the local minima, the optimization is done using genetic algorithms in MATLAB Global Optimization Toolbox. Still, at some volumes, the algorithm is not able to find the minimum, which causes peak points to the minimum energy curves. These error points were filtered to attain smooth energy curve.

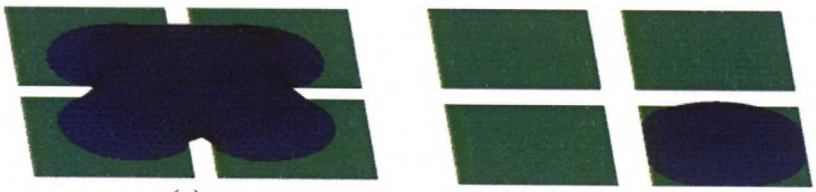

(a) (b)

Figure 23: Schematic of the wetting: (a) the droplet touching all four pads, (b) droplet slipping onto one pad.

The critical volume is calculated using (quasi) static simulations of liquid droplet's energy in Surface Evolver and optimizing the volumes of split droplets with genetic algorithm. Genetic algorithms search the optimal solution through combining and mutating the sets of parameters and using fitness function to choose the parameter sets which are more likely to get reproduced [46]. We used the implementation of the algorithm in MATLAB Global Optimization Toolbox.

First the total surface energy $E_{middle}(V)$ of one droplet in the middle of the pattern as a function of volume is obtained via simulations. Initial position of the liquid is symmetrically on the four-pad pattern, and thus evolving finds the local energy minimum in the middle of the pattern. Consecutive simulations are run with increasing droplet volume.

The total surface energy of single droplet on one pad as a function of droplet volume is then calculated in a similar way by setting the initial position of the liquid so that it covers only one of the pads. Since the resulting function $E(V)$ is not smooth due to numerical errors, it is smoothened with an averaging filter.

The goal of the optimization is to find the minimum total energy $E_{split}(V_{tot})$ as a function of total volume when there are multiple droplets. It is assumed that if there are multiple droplets on single pad they combine due to energy minimization.

For all of volumes V_{tot} in range 0.5 nl – 60 nl with 0.5 nl intervals, the volumes of the split droplets V_i are defined as

$$V_i = a_i V_{tot}, i = 1,2,3 \tag{14}$$

$$V_4 = (1 - \sum_i a_i) V_{tot} \tag{15}$$

Optimization of the droplet volume is done by optimising $a_i, a_i \in [0,1]$, i = 1,2,3, so that the total surface energy

$$E_{tot}(a_1, a_2, a_3) = \sum_{k=1}^{4} E(V_k) \tag{16}$$

is minimized. To get energy of volume between simulated data points in $E(V_k)$, linear interpolation is used. The scattering of the droplet on the pads with different volumes is visualized in figure 24.

When the optimal a_i , i=1,2,3 for certain volume V_{tot} are found, $E_{split}(V_{tot}) = E_{tot}(a_1, a_2, a_3)$ is the minimum energy for the split droplets with total volume

V_{tot}. Failed optimization causes peak points in $E_{split}(V_{tot})$, which are removed and replaced with the average of neighbouring values.

The critical volume is then obtained by finding the smallest volume where $E_{middle}(V) = E_{split}(V)$, as illustrated in figure 25.

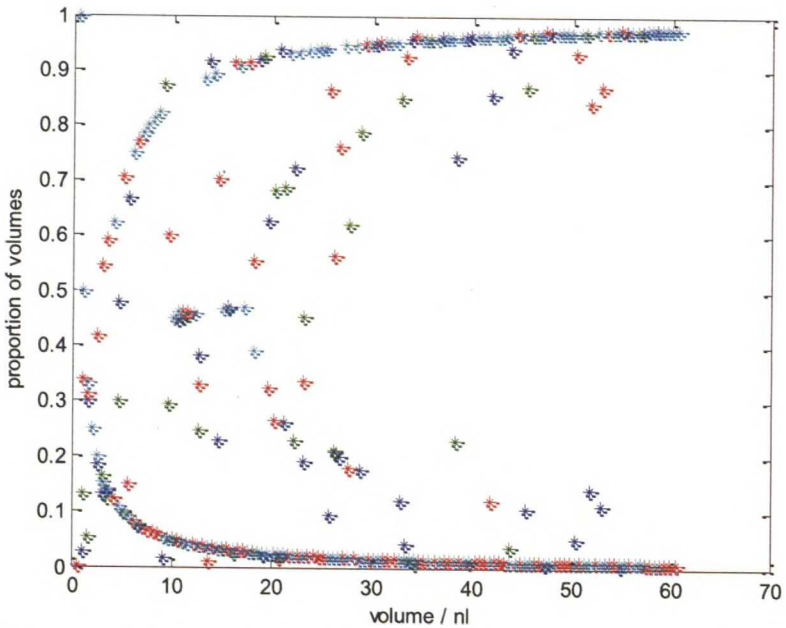

Figure 24: The optimal scattering of the water on four-pad pattern. The pattern size is 710 µm x 710 µm, gap size 10% of the pattern size (71µm), the contact angle with the pads is 41° and with the substrate 89°. Different colours represent the volumes of four droplets in percentages of the total volume.

In figure 25, the energy of scattered droplets and one droplet in the middle are plotted with respect to the total volume of the droplets. The sum of the energies of the split droplets is smaller than the energy of the droplet with the same volume positioned at the centre of the pattern, when the volume is smaller than the critical volume around 17 nl. Thus it can be predicted that the droplet will be likely to split when its volume is smaller than this critical volume. Likewise, the droplet will intend to stay in the middle of the pattern and wet multiple pads when the volume is larger than the critical volume.

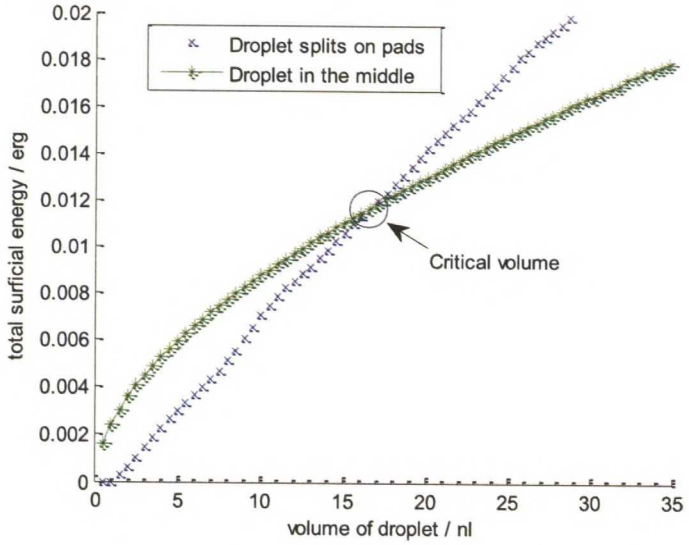

Figure 25: Energy comparison for the critical volume with 710 µm × 710 µm pattern, 71 µm gap and contact angles of 41° and 89° on the pads and on the substrate respectively.

Figure 26 shows the critical volume as a function of the relative gap, i.e. the size of the gap in percentages of the size of the pattern. Four contact angle pairs were chosen so that one of the pairs matches the contact angles of test pattern in [1], whereas the other pairs show the behaviour when one parameter at a time is varied. The results are non-dimensional and can be applied for any specific pattern size provided that the contact angles of the pattern are near to values in figure 26 and the length scale is smaller than capillary length of water. For a specific pattern size, the critical volume for the water to achieve good wetting is:

$$V_{critic} = (V_{ND} * A)^{\frac{3}{2}} \tag{17}$$

where V_{ND} is the non-dimensional volume from figure 26, corresponding to the relative gap in question, and A is the area of the pattern considered, as shown in figure 19.

In figure 26, the correlation between the size of the gap and the critical volume appears to be linear in range of gap sizes from 5 % to 30 % of the size of the pattern. In addition, when either the pads or the substrate become more hydrophobic, the critical volume increases. The effect of contact angles on e.g. the slope of the line is, however, not clear and the future work could consider the effect of contact angles more carefully.

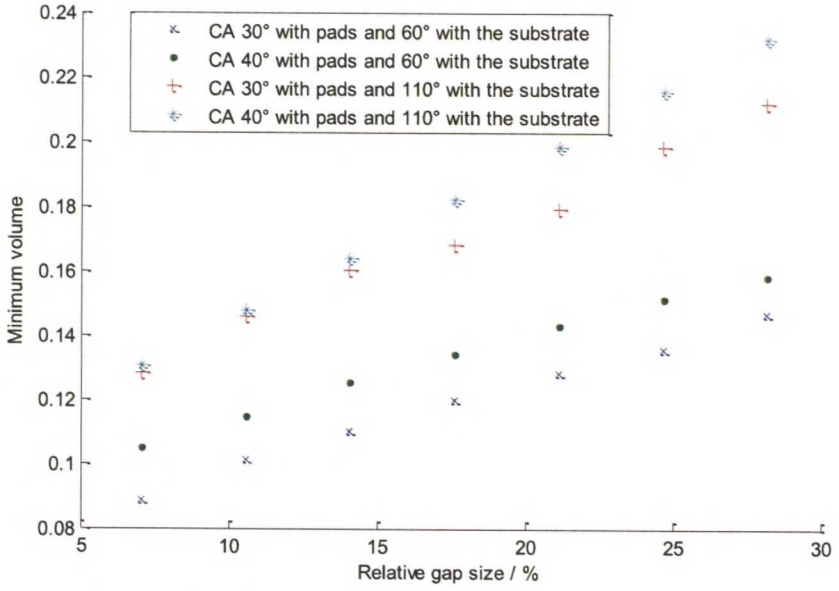

Figure 26: Non-dimensional critical volume with respect to the relative gap.

The model for wetting was created to give understanding about wetting on segmented patterns for experimental work, where the feasibility of self-alignment of RFID chips on four-pad patterns was studied, published in [1]. In the experiments, the contact angles of water on the pads and on the substrate were measured as 30° and 60° correspondingly based on the images as shown in figure 27. Consequently, the critical volume for different pad and gap sizes can be calculated by fitting a line to the data in figure 26 and using equation (17). Table 2 shows the critical volume for different combinations of the patterns sizes and the gap sizes.

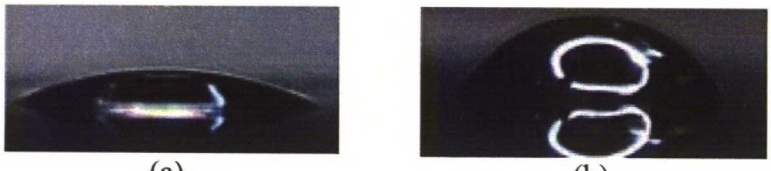

(a) (b)

Figure 27: (a) Contact angle of water on the pad: 30°. (b) Contact angle of water on the substrate: 60°

Table 2: The critical volume for test patterns in [1].

Pattern size (μm)	Gap size (μm)	Critical volume (nl)
710 × 710	50	9.8
710 × 710	100	12.9
730 × 730	50	10.5
730 × 730	100	13.8

4.3 Influence of the gap

During the self-alignment process, the bumps on the RFID die need to align with the corresponding pads which are separated by the gap. The size of the gap between the pads may have influence on the self-alignment process. Thus the self-alignment process is simulated using Surface Evolver.

To find out the minimum energy of the system at each step of self-alignment, the energy of the system is simulated with different gaps and initial biases in x-axis. Surface Evolver model is shown in figure 28.

In the simulation, the following assumptions were used:

- Partial wetting of the pads is allowed. Partial wetting is one of the reasons that the alignment may fail
- The droplet can spread outside the pads, when such spreading gives the minimum energy for the system
- The droplet can wet the bottom surface of the chip partially or fully
- The surface of the droplet may rise higher than the bottom of the chip when the surface in question is not under the chip;
- The distance between the chip and the target site, i.e. the z bias, is not fixed as the chip lies on water droplet and is free to move in vertical direction. Therefore, z bias is optimized by Surface Evolver in each simulation.

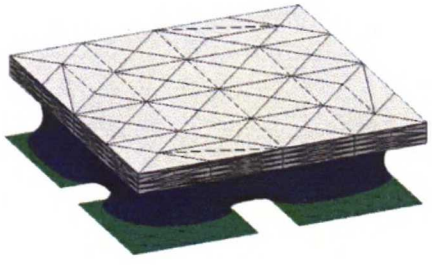

Figure 28: Surface Evolver model for self-alignment on four-pad pattern. The liquid may de-wet hydrophilic pads, and it may also spread to hydrophobic gap between the pads.

For comparison, self-alignment on four-pad pattern is also modelled using overlapping method as presented in section 3.1.2. The energy of the system then becomes

$$E(x,y,\alpha)=(\gamma_p-\gamma_s)A_{ol}(x,y,\alpha) \tag{18}$$

where x and y are the biases in x and y direction respectively, and α is the twist of the chip around z-axis. For simplicity, it is assumed that the twist of the chip is zero. Figure 29 shows the comparison of simulation and overlapping analysis results of the system energy with different biases. It is interesting to note that the simulated energy curves have similar shape but are delayed with a few micrometres from the results of overlapping analysis (18).

The restoring force acting on a chip is the slope of energy curve and can be calculated from

$$F_x = -\frac{\partial E}{\partial x} \tag{19}$$

where x is the bias in x-axis. When the bias is less than the size of a single pad, a larger gap leads to a lower slope in energy curve. Resulting low restoring force will cause the alignment to be more sensitive to disturbances and consequently lower yield at small biases. In addition, the self-alignment process is also likely to be slower. Nevertheless, the minimum energy state, i.e. perfect alignment, can still be reached otherwise.

Another phenomenon in figure 29 is that the curves have a flat part at certain range of initial biases. This leads to zero restoring force and the self-alignment may fail. Thus the flat part in the energy curve may give an insight to the largest allowable initial biases, which can be calculated according to overlapping model:

$$x_{\max} = \frac{l_{pattern} - l_{gap}}{2} \tag{20}$$

where x is initial bias, $l_{pattern}$ the length of the pattern in x direction and l_{gap} the size of the gap.

The results of overlapping model and simulation are further compared in a close-up in figure 30. The results for the energy calculated with (18) compare well with numerical simulation where the contact angles of the pattern and background are taken into account. Nevertheless, as seen in figure 30, the overlapping analysis is not able to fully capture the energy profile. This is because overlapping analysis doesn't account of the shape of the liquid due to different wetting properties of the pads and the substrate. In simulation, each flat part is delayed from overlapping model by 30 μm – 40 μm. This is also visible near the zero misalignment.

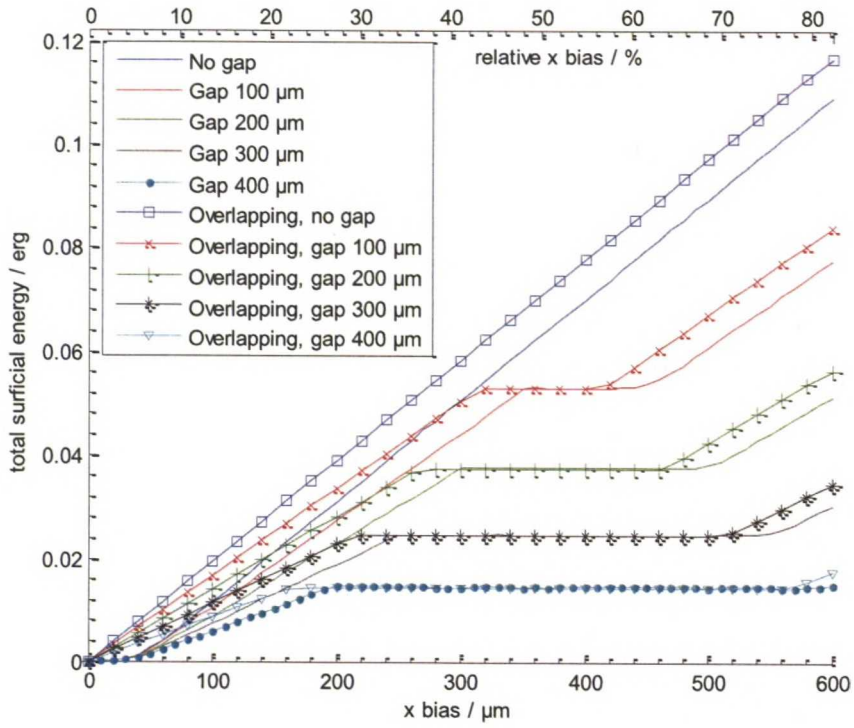

Figure 29: The energies from simulation compared with energy given by (18). The size of the pattern and the chip is 730 µm × 730 µm, and the contact angles are 30° with pads and 60° with substrate and the chip surface. The amount of water is 20 nl.

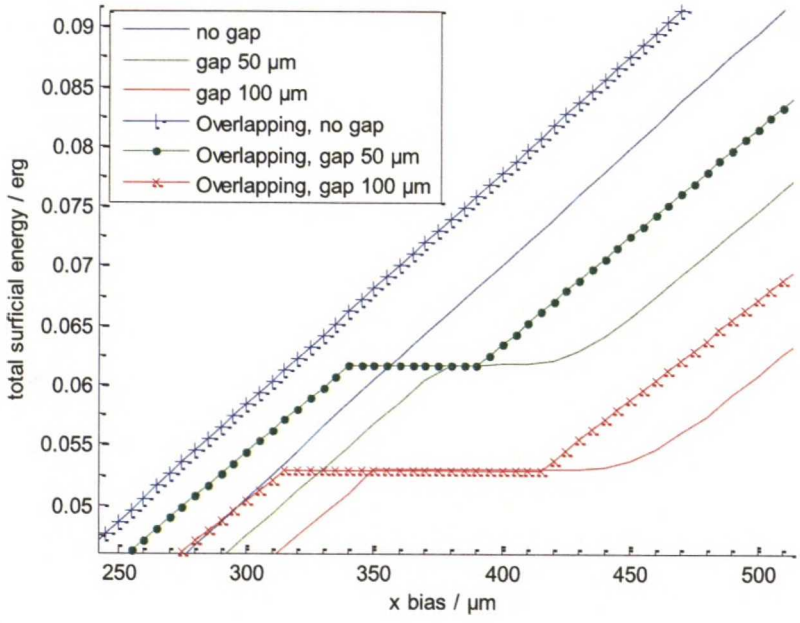

Figure 30: A close-up to show the flattening of the energy curves, compared with energy given by (18). The size of the pattern and the chip is 730 µm × 730 µm, and the contact angles are 30° with pads and 60° with substrate and the chip surface. The amount of water is 20 nl.

In figure 30 comparison of overlapping and simulation models shows that largest allowable biases with 50 μm and 100 μm gaps predicted by simulations are 380 μm and 350 μm, i.e. 52 % and 48 % of the size of the pattern correspondingly. These values are roughly 40 μm larger than the values predicted by overlapping analysis and equation (18). This can be explained by the shape of the liquid meniscus: the simple geometric model doesn't take into account the fact that the droplet is able to remain on two furthest pads even when the initial bias is larger than one pad, as illustrated in figure 31a. When the initial bias increases even more, the droplet is not anymore able to wet the pads, which is seen in figure 27b.

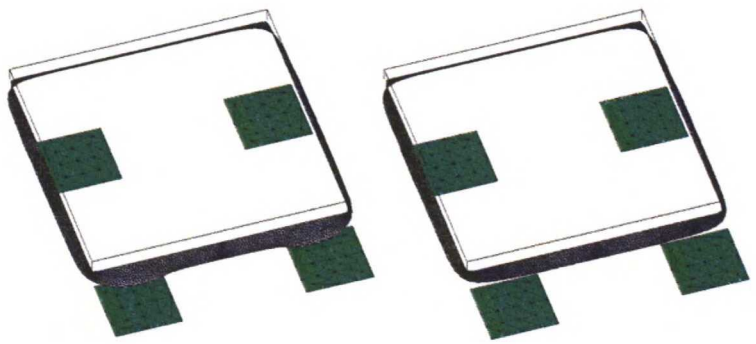

(a) (b)

Figure 31: The shape of the water meniscus with (a) 210 μm bias (b) 220 μm bias. Pad size 730 μm × 730 μm, gap 350 μm. Volume of the water droplet 20 nl, contact angle with pads 30° and with substrate and the chip 60°.

On the other hand, in section 3, the overlapping model was shown to be accurate when the bias is larger than the height of the liquid meniscus. Therefore I assume that the curvature of the liquid plays role in the range of liquid thickness. Thus it could be possible to estimate the delay of the flat part in energy curve by approximating the height of the liquid meniscus. The height of the liquid can be calculated by approximating the liquid shape with planar interfaces, as in section 3.1.1 When the pattern size is 730 μm × 730 μm and the volume of the droplet is 20 nl, the height of the liquid is 37.5 μm, which is close to the estimated delay between Surface Evolver and overlapping models.

The previous discussion of the energy and restoring force at one axis bias gives a good insight to the self-alignment process. However, initial biases in both x and y axes are involved in real-world process. It is interesting to check if two axes bias imposes other limitations for initial bias than the local minima discussed previously.

From the simulation results in figure 32, we can find that the restoring force in x direction decreases slightly if the chip is biased also in y direction. This will not, however, have a great importance at small x biases, since the setting is symmetric: if x-bias is large and y-bias is small, the small y-bias will be eliminated first and then the chip will align along one axis. If, on the other hand, the bias is large in both directions, the system is predicted to be more sensitive as the restoring forces are lower.

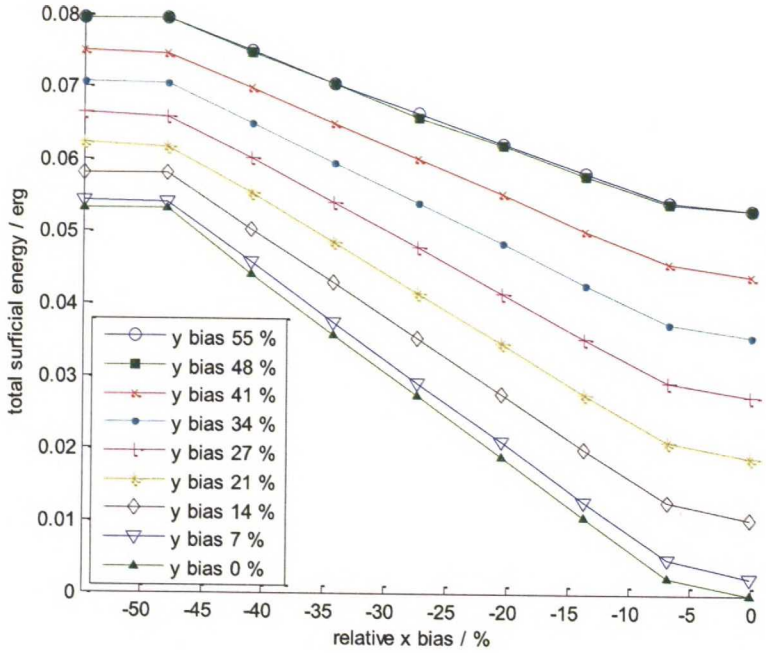

Figure 32: The energy with respect to the displacement in x and y direction. Gap size 100 μm, pattern 730 μm × 730 μm. Contact angles: 30° with pads and 60° with gaps and the substrate. The amount of water 20 nl.

4.4 Model validation

This section compares the modelling results with experimental results published in [1]. Since there is not method for directly measuring the capillary force, yield is used as indicator for the magnitude of the restoring force. Yield is the ratio of successful alignments to the number of experiments.

4.4.1 Validation of model for critical volume

The wetting of the segmented pattern can be studied experimentally by dispensing droplets onto pattern and analysing the wetting with different droplet volumes. The self-alignment pattern used in experiments in [1] were used for wetting tests to reveal the critical volume.

Figure 33 presents a few pictures from tests where critical volume was determined experimentally by dispensing droplets successively and capturing pictures right before and after the spreading to all four pads took place. The pattern has a contact angle of 40° due to aging. Due to the small volume of the droplet, the dynamic behaviour is different if the droplet is dispensed in one shot or incrementally, where incremental dispensing will usually lead to much larger volume due to the lack of impact which can help overcome the gap. Therefore, relatively large droplets were used to simulate the real-world scenario. However, this should still give a good estimation of the effective volume.

The average volume with standard deviation right before spreading is 27 nl ± 13 nl (19 repetitions) when droplet wets all pads. In case 1 of figure 33 very small amount of water was added precisely in the middle of the pattern and it shows clearly that with

careful control of dispensing, droplet with volume of 0.9 nl is able to wet all pads. This is, however, an extreme case and not feasible for self-alignment, and therefore those values for critical volume were not used for calculation.

Theoretically estimated critical volume for the same configuration as in figure 33 is 13.4 nl. This is close to the lower bound of the critical volume in experiments, which is 14 nl. The difference between experimental and theoretical values can be explained by the quasi static nature of the simulation, the dynamics are not considered, such as the contact angle hysteresis, the evaporation of liquid, the initial contact and delivery speed of the droplet. On the other hand, in self-alignment tests with 710 μm × 710 μm pad and 730 μm × 730 μm pad, 20 nl droplet was found suitable [1], which is slightly higher than the theoretical value, but smaller than experimental critical volume.

Both the theoretical and experimental values for critical volume are in line with the estimations of previous work [4], where optimal volume for 300 μm × 300 μm part was 1 nl – 3nl. Since the volume scales in l^3, as shown in section 2, the corresponding volume for 710 μm × 710 μm pad volume is 13 nl – 40 nl. This shows that the addition of gaps doesn't require significantly larger amount of water.

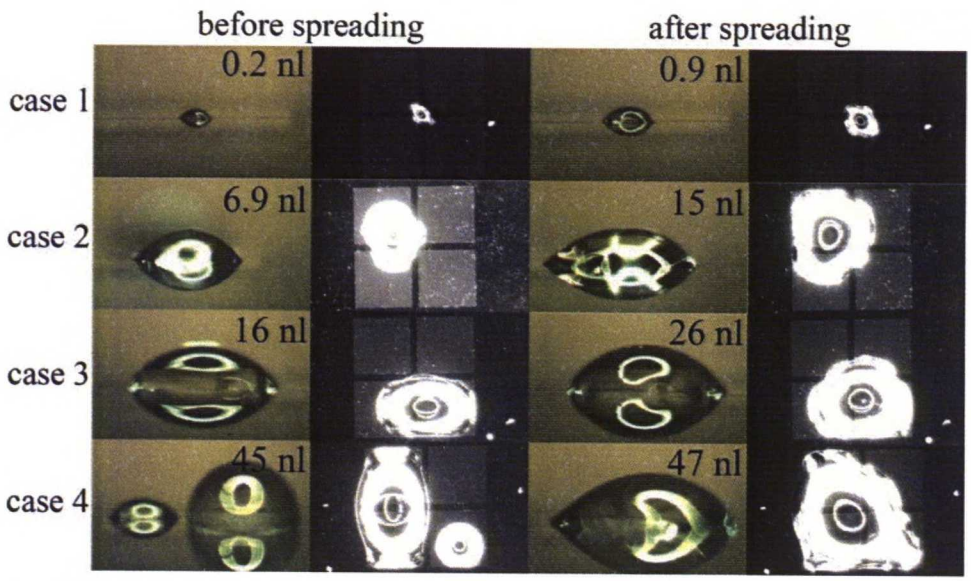

Figure 33: Wetting of segmented pattern with different volumes of liquid (pattern size 730 μm × 730 μm with 50 μm gap, contact angle 40° and 60° for the patterns and the substrate respectively). The pictures in each row are taken sequentially when more water is dispensed onto the same spot.

4.4.2 Validation of self-alignment model

In experiments in [1], the self-alignment was found to be successful even with large biases in both x and y directions, which can be seen from the table 3. It is interesting to notice that the maximum allowable initial biases predicted by simulation are 380 μm and 350 μm for patterns with 50 μm gap and 100 μm gap correspondingly (see figure 30). The experimental results show that an initial bias greater than the theoretical predication can lead to rather reliable assembly. This may due to the contact angle hysteresis of the droplet and the dynamics of the self-alignment process. At an initial bias greater than the maximum allowable initial bias, a meniscus may still exist between

the RFID die and the two pads supposed not connected to the meniscus according to the simulation model. Consequently, capillary self-alignment can still work. However, the restoring force may be smaller due to the local minimum at displacements around 50 % of the size of the die, which in this case corresponds to 365 μm bias. Therefore, even though the system is able to overcome the local minimum, the reliability of self-alignment is decreased.

However, the yield is not reduced in experiments with 400 μm bias at x-direction, which implies that the theoretical results are rather pessimistic. On the other hand, the experimental result for bias in both axes is rather similar to the simulation results, which can be seen in figure 34, where the yield is reduced when the bias is large in both x and y direction, and the total restoring force is lower.

Table 3: Yield of self-alignment in experiments, pattern size 730μm × 730μm [1].

x-bias, y-bias	50μm gap yield	100μm gap yield
50μm, 0 μm	100%	100%
100μm, 0 μm	100%	100%
300μm, 0 μm	100%	100%
400μm, 0 μm	100%	100%
500μm, 0 μm	80%	60%
600μm, 0 μm	0%	0%
50μm, 50 μm	100%	100%
100μm, 100 μm	100%	100%
200μm, -200 μm	80%	100%
300μm, -300 μm	20%	20%

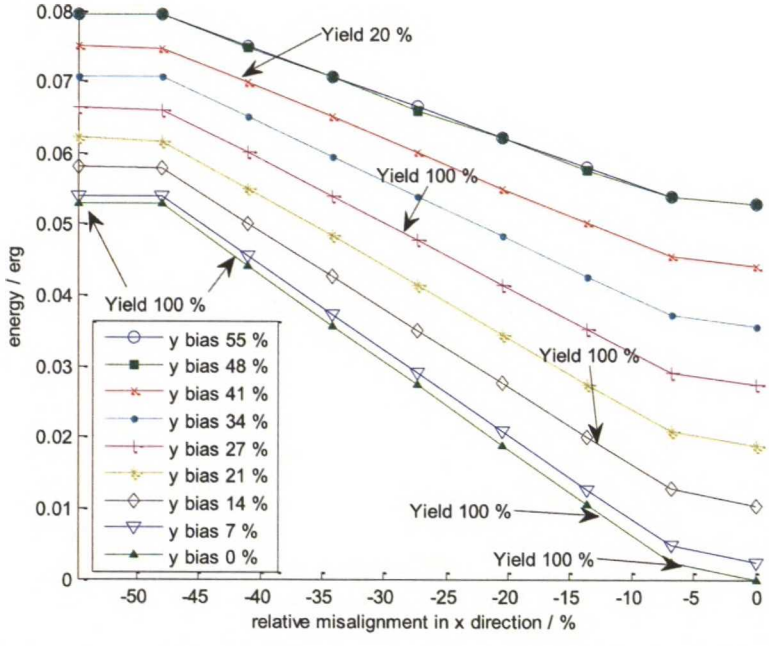

Figure 34: Comparison of simulated energy well with experimental yield from [1].

In conclusion, the theoretical analysis shows that the self-alignment is successful when the bias is smaller than one pad in segmented pattern. Furthermore, the comparison to experimental results showed that the alignment may be successful at even larger biases. Compared to the conventional solder self-alignment of micro-BGA (Ball Grid Array, BGA), where the allowed initial bias is known to be around 50 % of the size of one pad [41], the proposed technique enables self-alignment at much larger initial misalignments.

5 Simulator for chip path during self-alignment

The previous section analysed self-alignment on four-pad pattern using Surface Evolver model for finding the shape of the liquid meniscus. However, this iterative method is rather slow and computationally demanding for complex alignment pattern shapes. The model was also compared with simpler geometry based overlapping model, described in section 3.1.2, and the results showed only small deviation. Therefore more complicated configurations could be further studied using overlapping model.

In self-alignment experiments, as shown in figure 35, the chip normally rotates during the alignment. This twist has not been taken into account in Surface Evolver model in previous section, due to the complexity and extensive calculation it would have required. In addition to that, as discussed in section 4.4, in experiments [1] it was found that the self-alignment was sometimes successful even with bias larger than predicted by Surface Evolver simulation. Therefore a model that would easily consider all the process parameters, such as the twist, bias, shape of the pattern and chip, would be helpful. Hence a simple simulator based on overlapping analysis [25] is implemented.

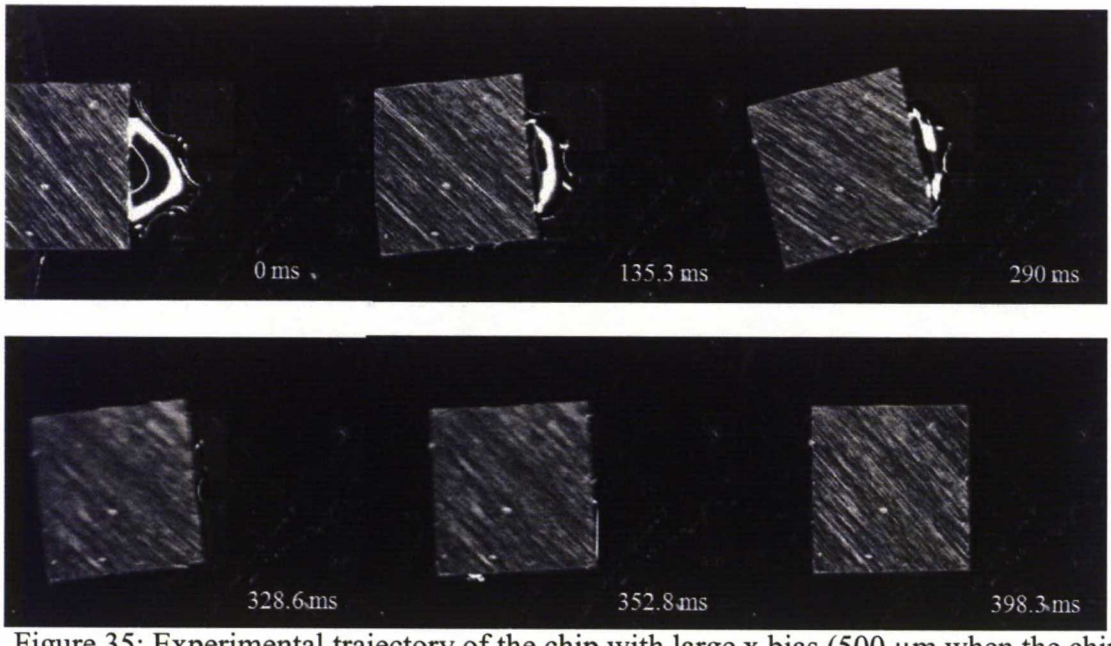

Figure 35: Experimental trajectory of the chip with large x bias (500 µm when the chip size is 730 µm × 730 µm) for the segmented pattern (size 730 µm × 730 µm with 100 µm gap). From [1].

5.1 Description of the simulator

In the simulator, the inputs are initial bias and pictures of chip and the pattern. The pictures of chip and the pattern are white shapes on black background, where white area defines the chip and pattern shape and size. Chip is free to rotate around z-axis and move in both x- and y-directions. At each step of the simulation, the position and orientation of the chip may change. The position containing also the orientation information is called pose.

To find trajectory from initial position of the chip, the algorithm firstly finds the energies of the neighbouring chip positions with ±1µm steps in x and y directions and

±1° steps in angular orientation. Then, the position of the chip is updated to the minimum energy position in that neighbourhood.

The algorithm for simulation is as follows:

1. Draw the current pose of the chip superimposed over the image of pattern
2. From memory, load the overlapping areas of points in current pose's neighbourhood
3. If overlapping area has not been calculated for some poses in the neighbourhood, calculate it and save it to the memory
4. Find the pose with maximum overlapping area in the neighbourhood, which then will be the new pose
5. Change current pose to the new pose

As a result, the simulator draws the path of the chip based on gradient of the energy: the step size is 1 pixel in lateral directions and 1 degree in orientation. With this simulator it is easy to analyse the success of self-alignment with various pattern configurations. The simulator also draws the graph that shows the energy level related to each poses on the alignment path. Example of simulated alignment path on four-pad pattern is shown in figure 36.

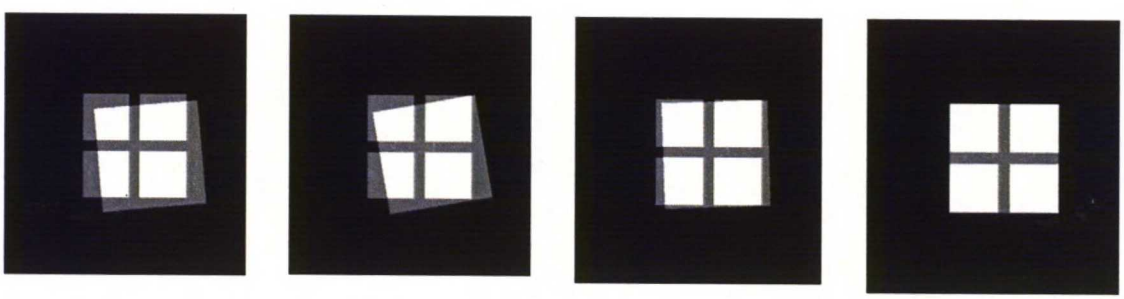

(a) (b) (c) (d)

Figure 36: Sequence of alignment in simulator. Gap 10 % of the size of the pattern (200 μm × 200 μm), initial misalignment 30 μm in x direction, 20μm in y direction and twist is 5°. (a) Initial position of the chip with respect to the segmented pattern. (b) Orientation of the chip changes during first phase. (c) Translational misalignment is left. (d) Chip is aligned.

5.2 Results and comparison to the experiments

The trajectory of square chip on square pattern is compared with experimental trajectory. Figure 37 shows that high-speed frames from self-alignment experiment and simulated trajectory are consistent. The trajectory does not take into account the speed of alignment, instead, movement at each step is -1μm, 0μm or 1 μm in x and y direction and -1°, 0° or 1° twist. Therefore, the time scale and steps are not linearly linked in figure 37.

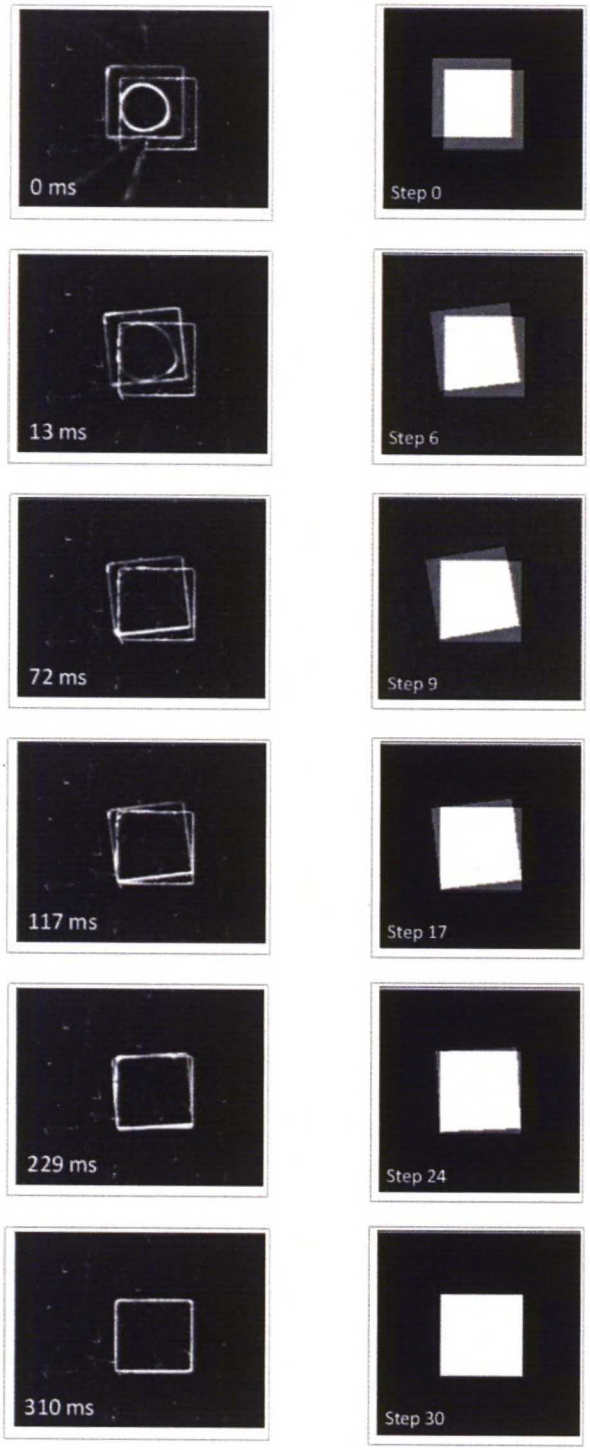

Figure 37: Trajectory of self-alignment from (a) high speed video frames (b) simulated trajectory.

The case with extremely large bias is simulated, and the trajectory and corresponding energy are shown in figure 38a. The bias is 65 % of the size of the

pattern in x direction, 30 % of the size of the pattern in y direction and twist is 5°. The size of the gap is 10 % of the size of the pattern. In figure 38, we see that when the chip starts to move, it twists more, so that the corner of the chip begins to overlap with lower right pad. Therefore the alignment is successful even when the size of the bias in x direction is larger than the size of the pad. This is seen also in energy curve in figure 38b, where the flattening of the energy curve is not as severe as in figure 29 and 30, which were simulated with Surface Evolver and did not take into account the twist of the chip.

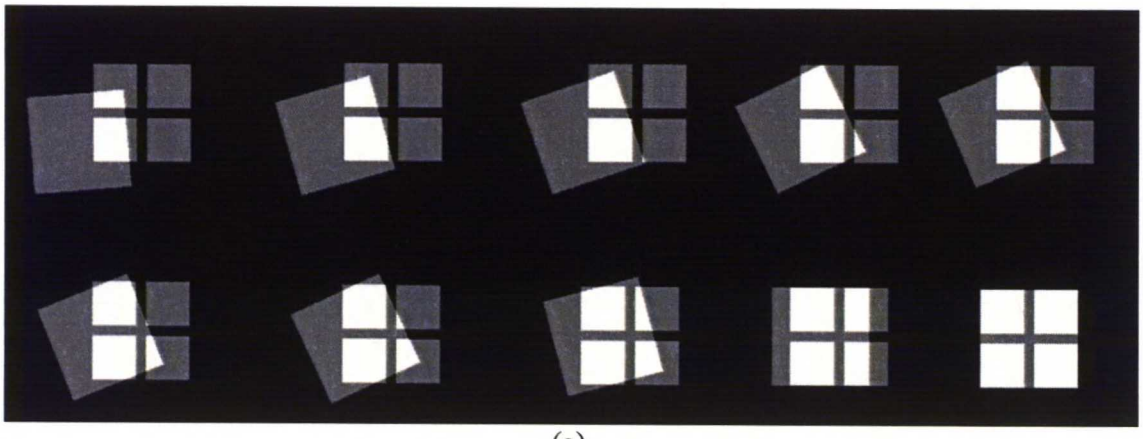

(a)

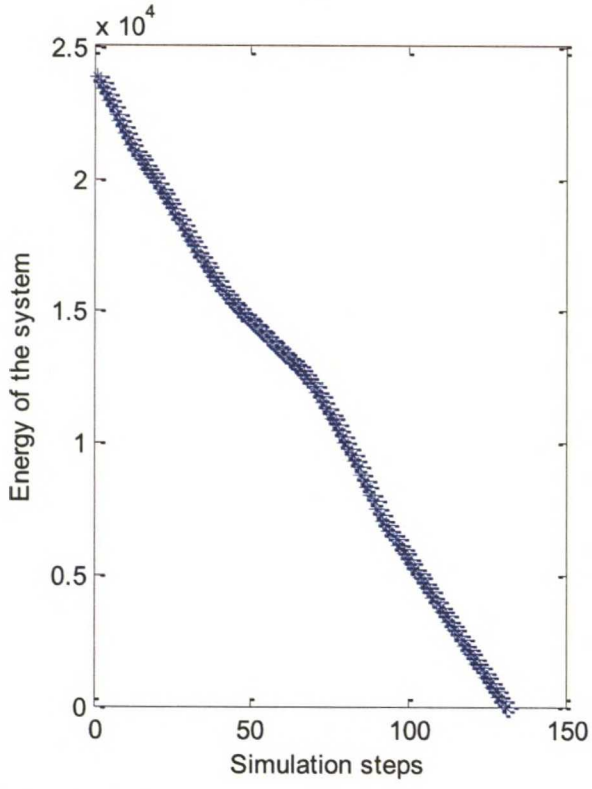

Figure 38: (a) Visualization of alignment with extremely large bias (65% of the size of the pattern in x direction, 30 % on the y direction and 5° twist). (b) Energy during the alignment. The effect of the gap is visible in reducing the slope of the curve, but twist of the chip prevents the alignment from being trapped in local minimum.

The comparison of the chip trajectory in figure 38a to experimental trajectory in figure 35 shows that similar twisting of the chip occurs when the bias is 500μm only on one axis. It is also good to note that the droplet wets initially all the four pads and the dewetting of the pads is not observed. This is in contradiction to Surface Evolver model, which predicts that the pads are dewetted when the bias is too large. This shows again the importance of the initial position of the droplet.

6 Self-alignment on poorly defined patterns

This section studies the influences of poorly-defined patterns on capillary self-alignment. The aim is to understand the relationship between the accuracy of the final alignment and the definition of the edges of the alignment patterns, or receptors, including single defects and multiple defects (or jaggedness). The results can reduce the requirements of design and manufacturing of receptor patterns in surface tension driven self-alignment process, which may eventually lead to lower cost of self-assembly and hybrid microassembly in applications. More relaxed requirements on receptor patterns also allow coexistence of self-alignment features and functional features of the device, and consequently reduce manufacturing complexity and improve the adaptability of self-assembly and hybrid microassembly.

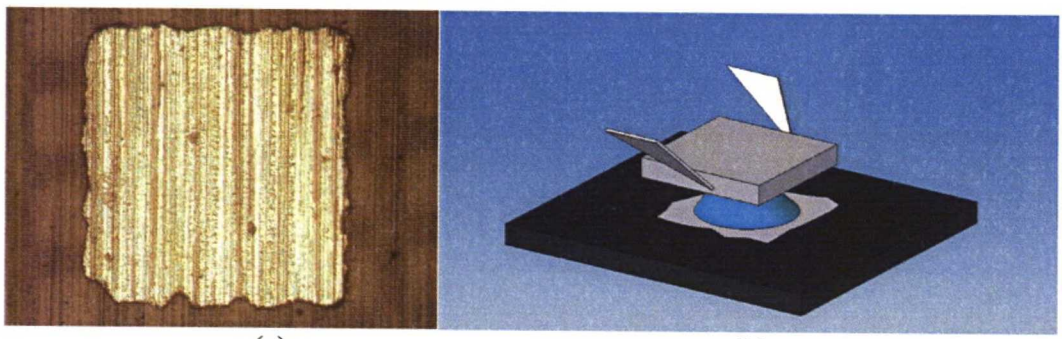

(a) (b)

Figure 39: (a) Jagged pattern in RFID antenna. (b) Schematic of alignment experiment on jagged pattern.

In related work, Lienemann et al. [32], [47] studied point-like defects in alignment patterns using Surface Evolver simulation. Their conclusion was that point-like defects do not affect alignment when they are located in the middle of the pattern, whereas defects on the edge of the pattern may impair alignment accuracy. Nevertheless, more experimental and theoretical work is needed in order to assess the performance of self-alignment on poorly defined patterns. In [48], [49] the alignment of the microchip on jagged patterns were studied experimentally. They found that self-alignment was successful on those jagged patterns, although the accuracy of alignment decreases as the jaggedness increases. Yet, the alignment accuracy was better than the pattern edge definition. To explain this, theoretical analysis is needed.

The theoretical analysis in next section has been designed and used together with experimental tests to understand the quantitative effect of jaggedness on alignment accuracy. The experimental tests are not in the scope of this thesis, and therefore they are described and discussed only briefly.

6.1 Poorly defined patterns with defects and edge jaggedness

In order to quantify the effect of imperfect edges on self-alignment, receptors with simple shape, namely squares, are used as the starting point. Squares are also the most used shape in microchips and many other cases. Two types of poorly defined patterns (also called low-precision patterns), are studied: the patterns with single defects and patterns with jagged edges, as illustrated in figure 40.

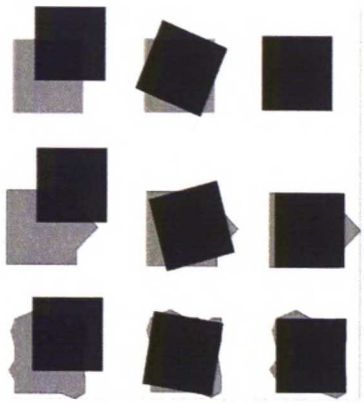

Figure 40: Self-alignment accuracy may be impaired due to defects in the alignment pattern or jagged edges of the pattern.

Firstly, the effect of a single defect is studied by varying its size, location, and direction. The direction refers to the addition or removal of area regarding to the original square, see figure 41. For the sake of mathematical simplicity, triangular defect shape is chosen, which is also similar to some real cases as shown in figure 39a.

Specifically, 6 types of patterns are chosen, as illustrated in figure 41b. This small sample population is chosen to reduce the amount of experimental tests where multiple repetitions are needed for each type and tedious accuracy analysis must follow for each test. The 6 types are grouped in three groups, A, B, and C. In each group, the patterns have the same size and location, but in different direction. Group A and Group C have the same location but different in size, from which we can evaluate the effect of size of defects. Group B has different location from group A and C, the size of group B is also between the size of group A and C. Therefore, we can interpolate the results of Group A and C and compare it with the results of Group B to understand the effect of location of defects. The size of the defect is defined by two parameters, the height h and width w of the defect, as shown in figure 41a. The aspect ratio of 2:1 is chosen for experimental patterns because it allows relatively high defects and it is close to the largest aspect ratio we observe in natural jagged patterns, e.g. in figure 39a.

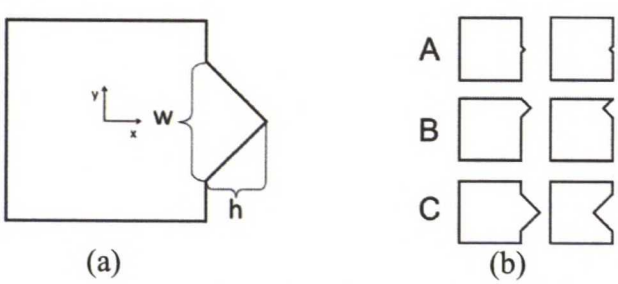

(a) (b)

Figure 41: (a) Design of the pattern with single triangle defect; (b) 6 different types of low-precision pattern with single triangular defect; Type A: defect in the middle, height 10μm width 20μm; Type B: defect at the upper corner, height 30μm width 60μm; Type C: defect in the middle, height 60μm width 120μm.The defect may be inward (right) or outward (left).

Two types of patterns with edge jaggedness have been designed, as shown in figure 42. The one on the left is of constant jaggedness, i.e. constant amplitude and pitch,

where pitch is also two times the amplitude. The pattern in figure 42a has random jaggedness, i.e. it consists of peaks with varying amplitude and pitch to amplitude ratio of 4:1 based on the observation of the pattern of a type of RFID antenna (figure 39a). More specifically, in the design of pattern with random jaggedness, the standard deviation of the amplitude varies from 1 to 4μm, and the pitches are always 4 times of the standard deviation of the amplitude.

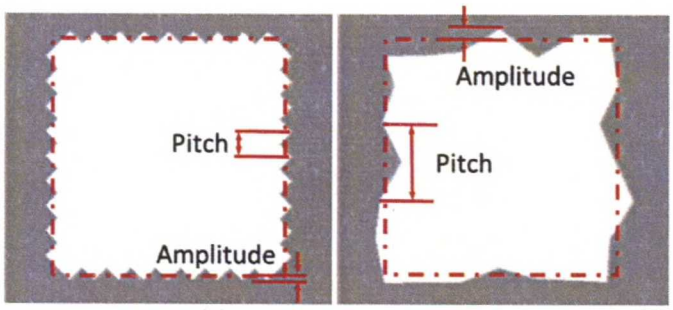

Figure 42: Two types of low-precision patterns with multiple defects. (a) Patterns with constant edge jaggedness with amplitude 4μm and pitch 8μm; (b) Patterns with random edge jaggedness with standard deviation of amplitude 8μm and pitch 32μm.

6.1.1 The accuracy of the alignment on poorly defined patterns

Self-alignment on patterns with single defect is modelled with overlapping model described in section 3.1.2. Figure 43 shows the flattening of the energy well with defects, compared to square pattern. The flattening indicates that the restoring force is lowered due to the defect in the patter. However, simple geometry based model shows that defects do not alter the alignment position, which is in contradiction with previous study of Lienemann et al. [47]. Therefore also Surface Evolver model is developed, since it takes into account the wetting of the defect and the height of the liquid layer.

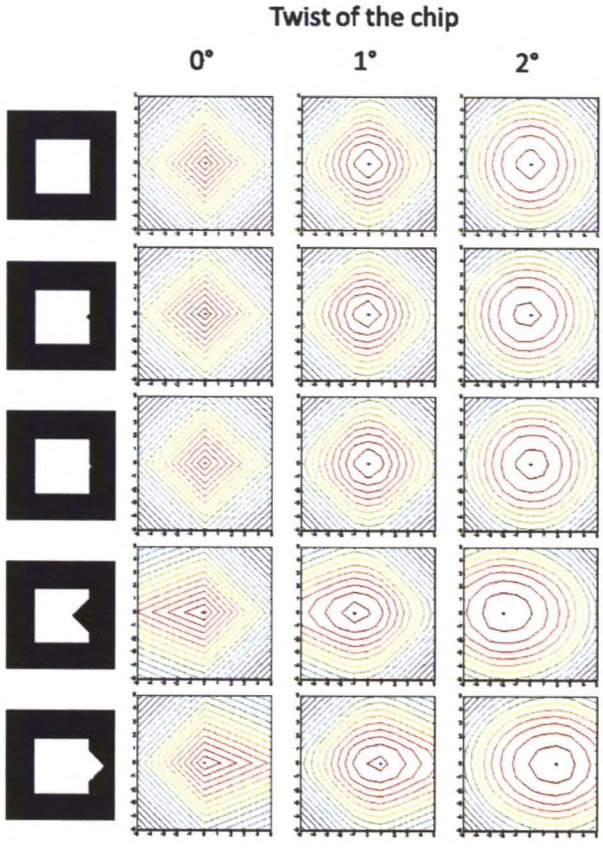

Figure 43: Energy landscape of different patterns, and how twist of the chip changes it. For each twist, minimum energy position is marked with dot. Total minimum energy (red dot) is found at x = 0, y = 0, twist = 0 regardless of the defect. The scale in each square is from -5μm to 5μm in x and y axis.

In a Surface Evolver model, shown in figure 44a, the twist of the chip is not simulated when the pattern is symmetric with respect to the axis of movement. This is justified by the figure 43, which shows that the alignment without twist always results in smallest energy. Since the background in experiments is superhydrophobic, it is assumed that the liquid does not overflow. Therefore overflow is not allowed and the droplet is constrained inside the pattern. The only exceptions to this are the patterns with inward defects, where the contact angle on the defect area is set to 180°, because the simulation run into numerical problems otherwise. Therefore the liquid may, if energetically favorable, wet also super-hydrophobic area. In the model, the liquid may de-wet sharp corners on hydrophilic alignment pattern.

Figure 44b shows the x-error for different defect sizes and aspect ratios, simulated by Surface Evolver. The x-error is the difference in centres of the chip and the pattern in x-axis after the self-alignment. The accuracy of the alignment is plotted against the area of the defect, which shows that the x-error increases with increasing area of the defect: with outward defect (with aspect ratio 1:4) x-error is 2 μm for defect area 1500 μm² and 6 μm for defect area 4000 μm². Moreover, scaling of area in l^2 would predict the larger defect to cause error of 3.3 μm. The conclusion is that the area of the defect is not enough for determining the misalignment due to the defect. The simulation results indicate also that the aspect ratio 1:4 (height to width) causes largest error, and the error

decreases as the aspect ratio increases. Another phenomenon in figure 44b is that the inward defects cause less misalignment than the outward defects.

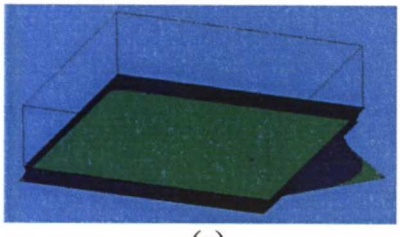

(a)

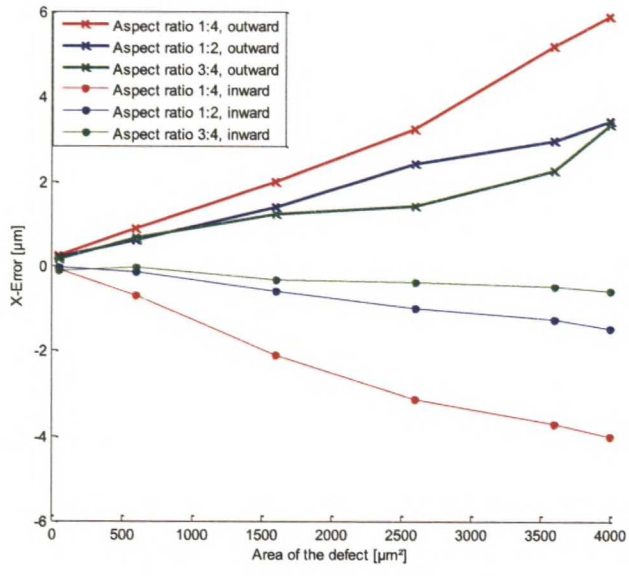

(b)

Figure 44: (a) Surface Evolver model for single defect (outward, pattern type A). (b) Simulated accuracy of the self-alignment on patterns with single defect, inward and outward defect, volume of the droplet 0.5 nl and pattern size 200 µm × 200 µm.

When the defect is located in the corner of the pattern, it is likely to cause rotational error to the alignment due to asymmetric shape. Figure 45 shows the method for finding the accuracy on patterns with defect in the corner (pattern type B in figure 41b). In figure 45, the energy of the system with different twists of the chip is simulated. During the simulation, Surface Evolver optimizes the x-position of the chip so that the energy is minimized. Then, the x-position of the chip is plotted as well, so that x-error is found at the twist where the energy is at minimum, shown with arrows in figure 45.

From figure 45, the x-errors for patterns with defect in the corner (height 30 µm and width 60 µm) are 1.5 µm in x direction and 1° twist clockwise for outward defect, and for inward defect -1 µm in x direction and 1° twist counterclockwise. On the contrary, the maximum overlap on those patterns is found when there's no twist of the chip and no misalignment either. This shows that Surface Evolver results are different from results of overlapping analysis, as Surface Evolver is able to estimate the misalignment due to the defects.

In conclusion, the simple overlapping model shows the decrease in restoring force when there are defects on the edges of the pattern. However, only Surface Evolver model can estimate the accuracy of the alignment. The results from Surface Evolver model show that the misalignment caused by the defect is smaller in scale than the size of defect, for instance, the largest simulated x-error is 6 µm, which is achieved when defect width is 179 µm and height 45 µm. This was also observed in previous study [48].

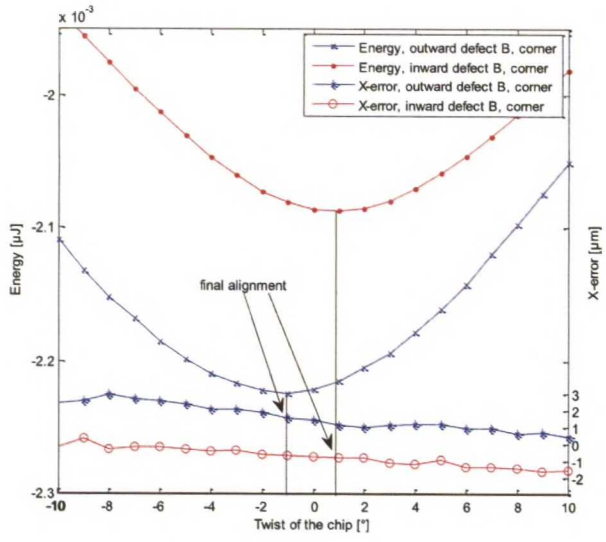

Figure 45: Self-alignment on patterns with defects in the corner (pattern type B), simulated with Surface Evolver. The final alignment position is found where the energy is at minimum (arrows in the figure). For outward defect with height 30µm and width 60µm the twist of the chip is -1° (clockwise) and the x-error 1.5µm and for inward defect with same size, the twist is 1° (counter clockwise) and the x-error is -1µm. The volume of the droplet 0.5nl and the size of the pattern is 200 µm × 200 µm.

More complicated shape of the poorly defined pattern consists of multiple defects on the edges. This is modelled by two types of jaggedness, constant and random jaggedness. To be able to simulated edge jaggedness with Surface Evolver, sinusoidal edge shape is used to represent constant edge jaggedness. Figure 46 illustrates the Surface Evolver model of self-alignment of a chip on a receptor with constant edge jaggedness.

Figure 46: Surface Evolver model of self-alignment constant edge jaggedness on alignment pattern, amplitude 8µm.

In order to quantify the effect of constant jaggedness, the self-alignment on patterns with constant edge jaggedness is simulated with varying jaggedness amplitude. Figure 47 shows that restoring force decreases when amplitude increases, but the final position of the chip is unchanged from that of patterns without jaggedness. On the other hand, the decrease in restoring force indicates, as previously with four-pad patterns, that the alignment reliability may not be as good on jagged patterns as with perfectly defined alignment patterns.

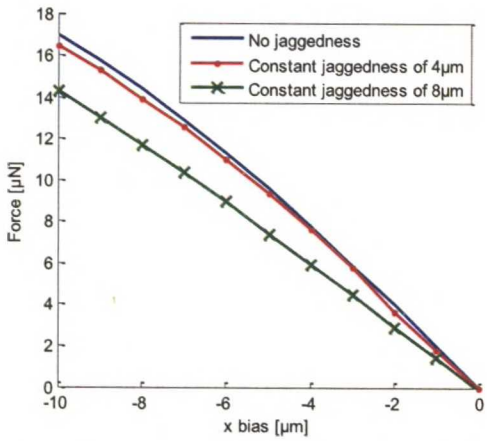

Figure 47: Restoring force with constant edge jaggedness. The chip and pattern size is 200μm × 200μm. Volume of the droplet is 0.5nl.

When random edge jaggedness is simulated, the simulator for chip trajectory is used in order to avoid complicated pattern definition and numerical complexity in Surface Evolver. The alignment trajectory is simulated from initial bias similar that will be used in experiments. The energy during alignment is shown in figure 48. The energy curves in figure 48 flatten at the end of the alignment, except for the pattern without the jaggedness. This shows that the restoring force decreases at the end of alignment, as predicted by Surface Evolver results for constant jaggedness as well. However, in the case of random jaggedness, the final position of the chip is also altered, which is explained by the random shape of the pattern. The randomly jagged edges distort the original pattern so that the maximum overlap is not found at zero misalignment. The values for final misalignment are shown in figure 48: for 2 μm jaggedness they are x: 0 μm, y: 1 μm, α : 0°, but for jaggedness 8 μm, x: 5 μm, y: 5 μm and α : 1°.

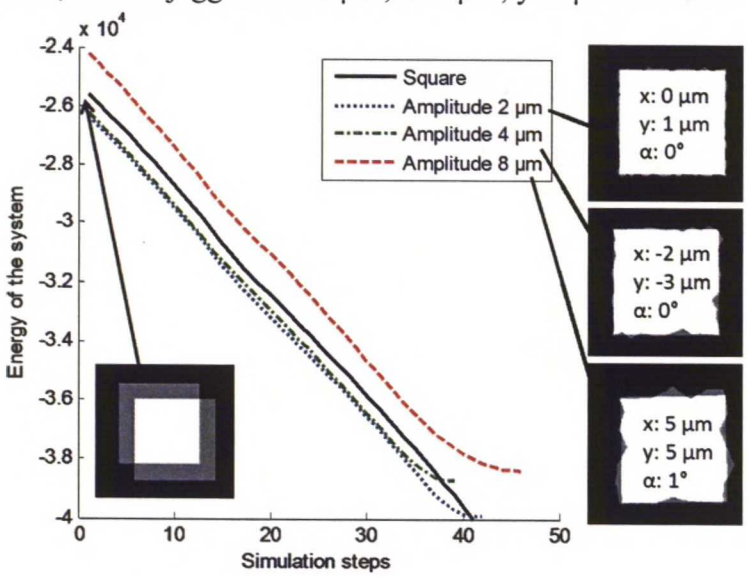

Figure 48: The energy of the system during alignment of the chip on patterns with random edge jaggedness of varying size. Initial bias in x and y axis is 40μm, as shown in inset with square pattern. The final chip poses are shown in insets on the right.

6.2 Model validation

For model validation, experimental tests are done in hybrid assembly station. In this section, the experimental set-up is described briefly. Then the measurement method for alignment accuracy using Scanning Electron Microscope (SEM) is described, and the experimental results are compared with modelling results from previous section.

6.2.1 Description of the experimental set-up and methods

A hybrid microassembly station (shown in figure 4) is used to carry out the experimental tests. It has two microscopes (Edmund/VZM1000i) for top view and side view. A piezoelectric microgripper (MicroTec2003) is used to pick-and-place test chips and a 2DOF stage moves the sample (Physik Instrumente M-122.2.1DD and M-404.8PD). A non-contact dispenser (Gesim/PicPIP) can dispense water droplet down to 300 pl. The system has also contact dispenser (EFD Mikros pen system) which can be seen from the second sideview microscope (Edmund/VZM300i). Contact angles of droplet can be measured from side-view microscope images of dispensed droplets where the non-contact dispenser is used for dispensing water on hydrophilic patterns and contact dispenser is used to measure contact angle on superhydrophobic substrate.

For surface tension driven self-alignment, hydrophilic receptor on hydrophobic background are needed. Hydrophobic background is achieved using black silicon coated with hydrophobic fluoropolymer [19]. The hydrophilic patterns are silicon, with native oxide grown on top of them. The chips used in tests are SU-8 photoresist dummy chips with thickness of 50μm. SU-8 is polymer photoresist, which is patterned using lithography in standard SU-8 50 processing. The contact angles are listed in Table 4.

Table 4: Contact angle of water on pattern and substrate

Advancing contact angle on patter	Receding contact angle on patter	Advancing contact angle on substrate	Receding contact angle on substrate
50°	31°	171°	159°

Receptor with both single defects and edge jaggedness are fabricated for the experimental tests. Figure 49 shows a 200 μm×200 μm receptor with single triangular defect, both outward (figure 49a) and inward (figure 49b). Figure 50 shows a 200 μm × 200 μm receptor with constant edge jaggedness (figure 50a) and a 200 μm × 200 μm receptor with random edge jaggedness (figure 50b).

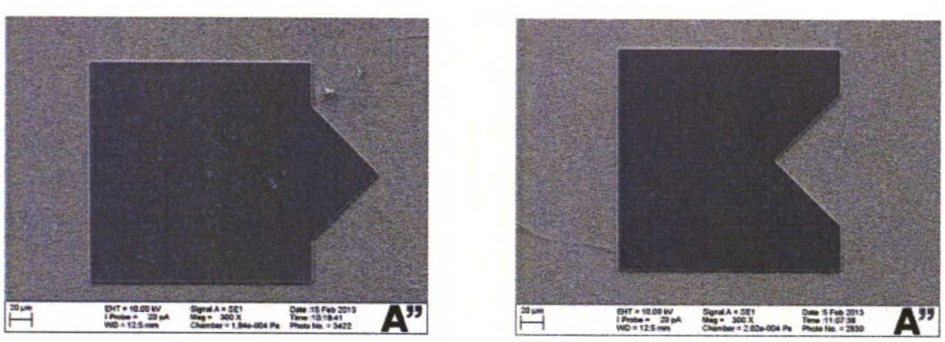

(a) (b)

Figure 49: Microfabricated 200 μm × 200 μm patterns with a single triangular defect (height: 60 μm, width: 120 μm): (a) outward defect; (b) inward defect.

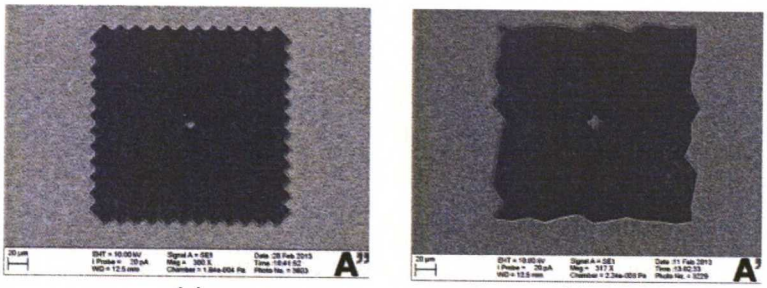

(a) (b)

Figure 50: Microfabricated 200 μm × 200 μm patterns with (a) constant edge jaggedness (amplitude: 4 μm, pitch: 2 μm), (b) with random edge jaggedness (standard deviation of amplitude: 4 μm, pitch: 16 μm).

The experiments are done by dispensing the water droplet on the test pattern, and then bringing the microchip in contact with the droplet, with pre-defined initial bias 40 μm in x and 40μm in y direction. Releasing height is 40 μm. The volume of the droplet is 0.9 nl. After the chip is released by the gripper, the droplet self-aligns the chip with respect to the pattern. Each pattern type with different jaggedness is tested at least 5 times. Experiments are done in ambient room environment.

6.2.2 Measurement method

The accuracy of the self-alignment is measured using a Carl Zeiss EVO HD15 LS environmental scanning electron microscope (ESEM) with LaB6 electron source. The microscope has a specified resolution of 3 nm using 30 kV acceleration voltage in a variable pressure environment.

To check the accuracy of SEM measurements, an image of reference sample (Bruker AFM Standard 10-10299) is taken first. The reference sample dimensions are known, and they are compared to measured dimensions in calibration images. The error in SEM measurement was found to be less than 1% in the calibration images when working distance was kept constant and hysteresis was removed. Without these precautions the error could exceed 10%, so these steps were made each time before imaging the new batch of samples.

The rotational error is measured from top view images as shown in figure 51. First, the orientation of empty pad is measured, and that is compared to the orientation of the chip, which is found automatically using machine vision. Misalignment in x direction is measured from side view images (stage tilted 85°, angle of the view as in figure 52a) by measuring the distance between chip and pattern corners, as shown in figure 52b-c, and removing the effect of twist from these measurements. The twist removal, illustrated in figure 53, is done by calculating the distance between chip and pattern corners, caused by the twist. Then this value can be subtracted from measured difference between corner positions, so that real x-error is found.

The measurements are made from both left and right side, which results in two values for x-error for one test sample. These values may differ from each other due to measurement error or the size difference between the chip and the pattern. In order to decrease the effect of measurement error, the average of x-error on the left and right is

used for calculating the final x-error. Furthermore, the size difference can be calculated by calculating the difference between left and right measurement for x-error.

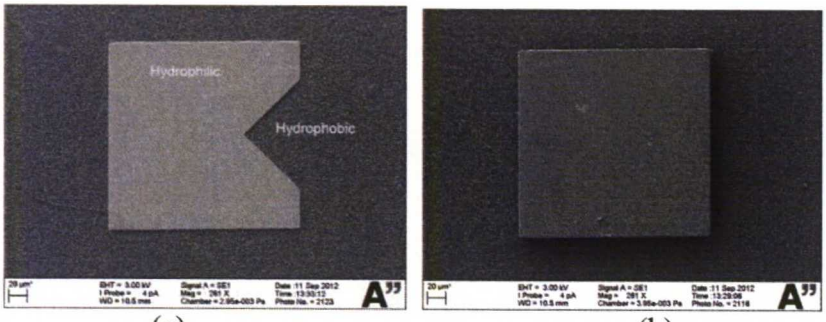

(a) (b)

Figure 51: Alignment accuracy measurement in SEM. (a) The orientation of the empty pattern is measured. (b) The orientation of the chip is measured and compared with that of the pattern to calculate the rotational misalignment. The size of inward defect in the middle of the edge: height 60 µm, width 120 µm.

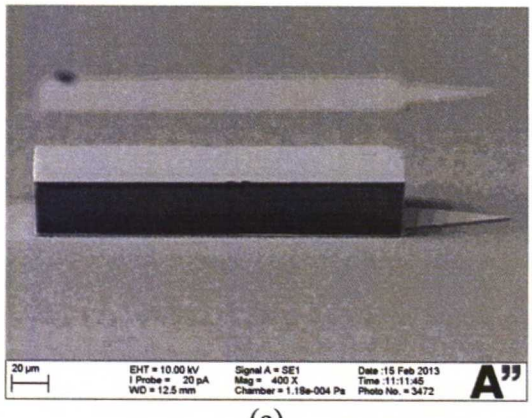

(a)

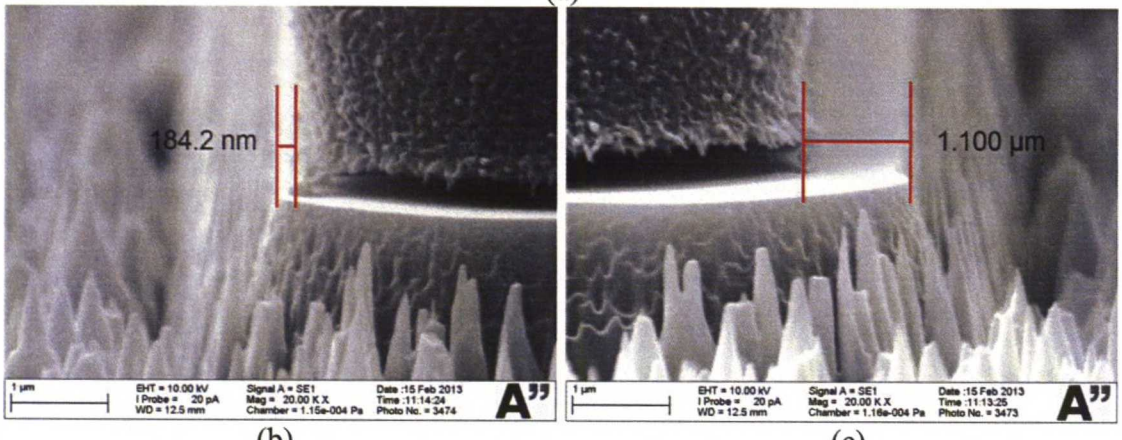

(b) (c)

Figure 52: (a) Sideview of aligned chip: outward defect (height 60 µm and width 120 µm) on right pattern edge is visible in the figure. (b) Left and (c) right closeup of the aligned chip corneres. The left and right close-up side views are used to measure the x-error and size difference between the chip and the pattern. The effect of the twist is removed from the measurements in order to find the real x-error. The difference between left and right measurement is the size difference of the chip and the pattern.

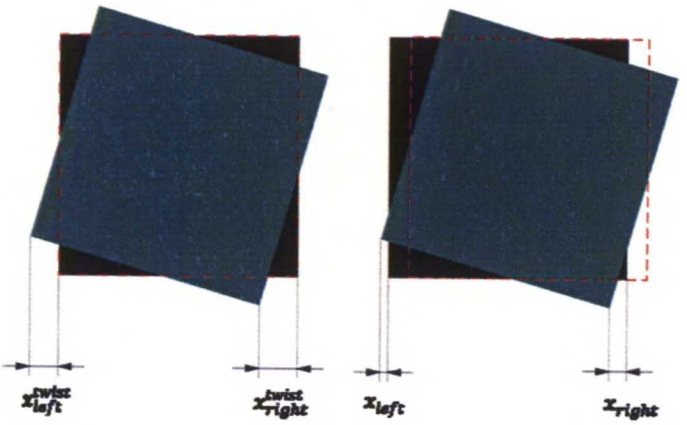

Figure 53: Twist of the chip causes error in measurement of lateral misalignment. The square marked with red dashed line is the position of the chip without the twist. When the twist is known, the error from twist (x_{left}^{twist} and x_{right}^{twist}) can be removed from measurements (x_{left} and x_{right}) to find out the lateral misalignment of the chip.

6.2.3 Comparison of model with experimental results

The alignment accuracy on receptors with single defects or edge jaggedness was studied. In this section the results of experiments are presented and compared with theoretical simulations in the subsections below.

6.2.3.1 Single defect

Self-alignment tests for single defect receptors have been done for all six pattern types, showed in figure 41b. The experiments were repeated so that there were 10 successful alignments for each pattern type. One example of self-alignment on pattern with single defect is shown in figure 54, and typical alignment results, viewed in SEM, are shown in figure 55.

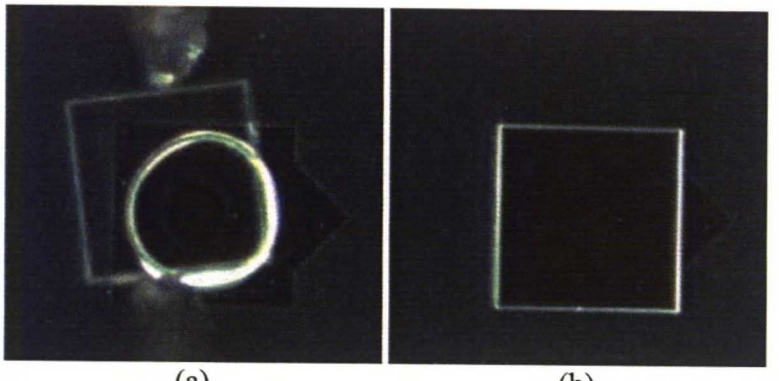

(a) (b)

Figure 54: Self-alignment of a 200 μm × 200 μm SU-8 chip on a matching pattern with single ouward defect: a) a chip is brought nearby a pattern and ready to be released, (b) the chip is aligned with the pattern.

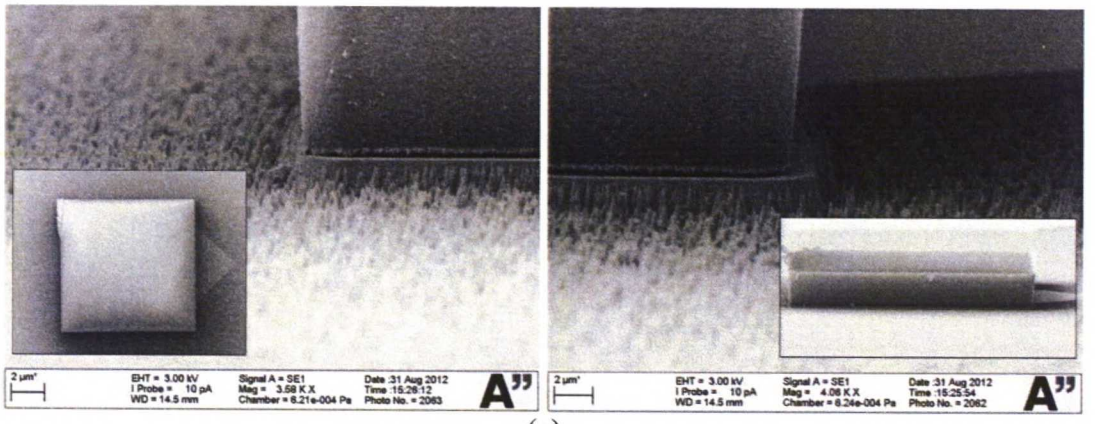

(a)

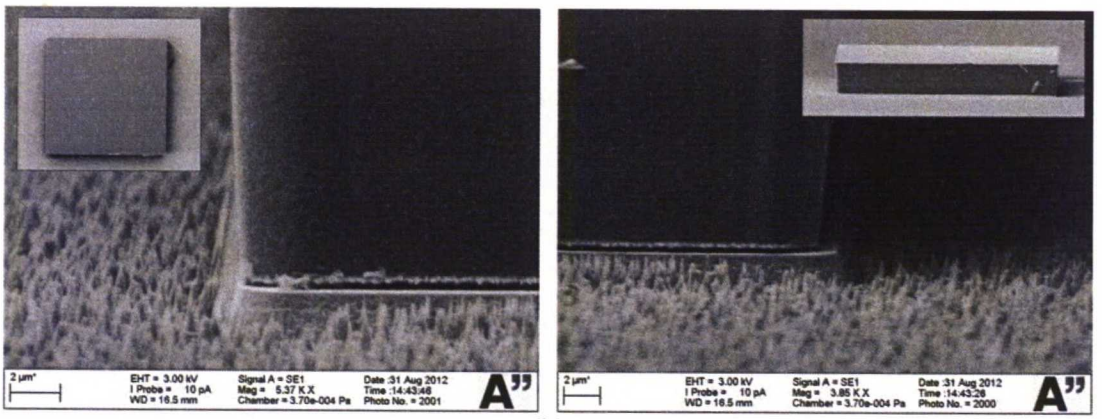

(b)

Figure 55: Typical alignment results with accuracy better than 1 µm. Insets show overview images from top and side. (a) Pattern type C, outward defect. (b) Pattern type B, outward defect.

The alignment accuracy has been observed using ESEM, and the results are shown in figure 56. They show that the translational misalignment is related to defect size. X-error increases with the increased defect size, although high accuracy of 2 µm ± 1.5 µm can still be achieved even with outward defects as high as 60 µm and wide as 120 µm. Figure 56 shows that there is statistically significant rotational misalignment regardless of the position of the defect in 10 µm high inward defect in the middle and 30 µm high outward defect in the corner. However, there might be systematic measurement error that accounts for that 0.1° rotational misalignment. Compared to the previously reported accuracies with matching chip and patterns (0.2 µm for lateral and 0.3° for rotational accuracy [2]), defects with height 10µm and width 20µm cause similar magnitude of error.

When the experimental results are compared to Surface Evolver results from section 6.1.1, the rotational error for pattern type B is slightly smaller in experiments than in simulation, but the direction of the twist is the same. Experimental twist is -0.1° ± 0.1° for outward and 0.5° ± 0.5° for inward defects, whereas the simulated twist is -1° for outward and 1° for inward defect. Also the x-error for outward defects is smaller in experiments than in simulation. On the contrary, the experimental results are well in line

with simulations of inward defects: for inward defect the simulated error is -1 μm, whereas the experimental error is -1 μm ± 0.4 μm.

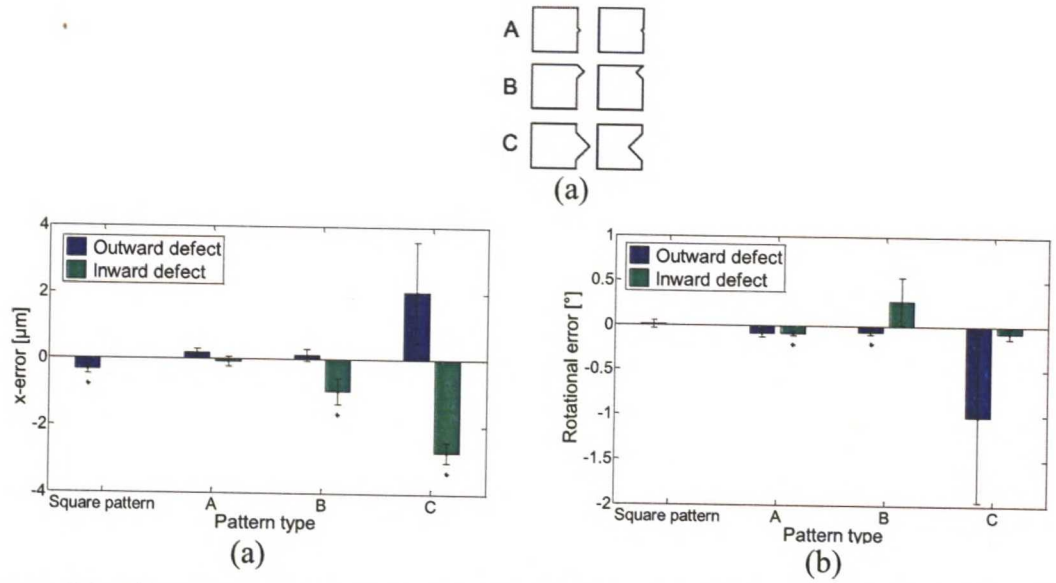

Figure 56: Alignment accuracy on pattern with defect. Defect area increases to the right. The mean of (a) x-errors and (b) rotational errors measured from experiments, errorbars corresponding to standard error of the mean. Marked with (*): in Student's *t*-test, the p value is less than 5%, meaning that the mean differs significantly from zero. Tests were repeated 10 times for all pattern types, except for outward B pattern, where one chip detached before imaging and only 9 samples were analysed.

Experimental results are further compared with Surface Evolver results for lateral accuracy of alignment in figure 57. It can be found that for droplet volume 0.9 nl, which was used in experiments, the simulation overestimated the misalignment, whereas for a smaller volume (0.45 nl) the theoretical results are closer to experimental results. This may be caused by the evaporation during self-alignment experiments, which decreases the droplet volume.

In summary, the effect of single defect on self-alignment accuracy is smaller than the scale of the defect: when the width of the defect is 60% and height is 30% of the pattern edge length, caused lateral error is less than 2% of the length of the chip edge.

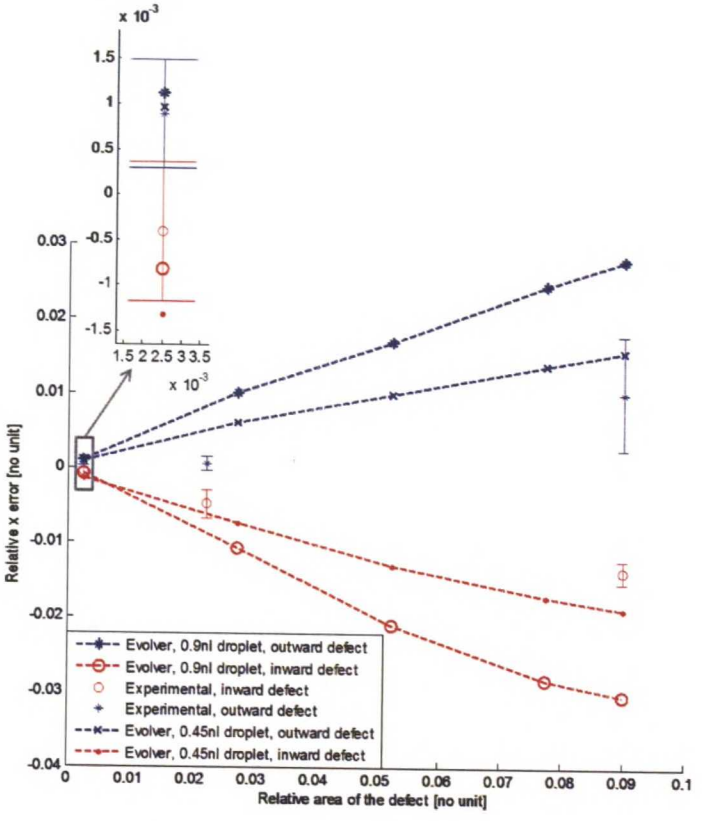

Figure 57: Relative alignment accuracy (x/L, where x is the x-error and L is the length of the edge of the chip) with respect to the relative defect area ($A_{defect}/A_{pattern}$, where A_{defect} is the area of the defect and $A_{pattern}$ the area of the pattern without defect), for inward and outward defects. Surface Evolver results are plotted with dashed lines for comparison, with two different droplet volumes. Experimental results are mean values from experiments, errorbars showing standard error of mean. In simulation, the contact angle on the pattern is 31°, which is same as measured receding contact angle of patterns in experiments.

6.2.3.2 Patterns with jagged edges

Next, the models for constant and random edge jaggedness are compared with experimental results, and the differences of Surface Evolver model and trajectory simulation are evaluated. In section 6.1.1 constant edge jaggedness was simulated using Surface Evolver, and the results indicated that constant jaggedness does not impair alignment accuracy, although it decreases the restoring force.

Four different size of constant jaggedness were tested: amplitudes 1.7 μm, 3.2 μm, 5 μm and 15 μm. Figure 58a,b shows one example of a 200 μm × 200 μm SU-8 chip assembled on a 200 μm × 200 μm pattern with constant jagged edges of amplitude of 3.2 μm. Figure 58c,d demonstrates the 200 μm x 200 μm SU-8 chip assembled on the 200 μm × 200 μm pattern with constant jaggedness of extremely large amplitude of 15μm. Each pattern type was tested at least 5 times.

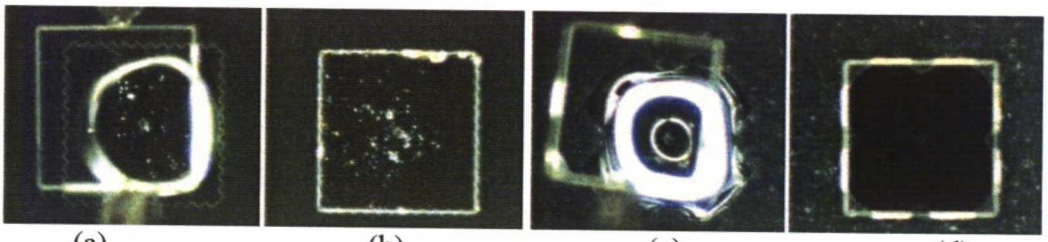

(a) (b) (c) (d)

Figure 58: Self-alignment of a 200 μm x 200 μm SU-8 chip on a matching pattern with constant jagged edges of (a,b) 4 μm amplitude and (b,d) 15 μm amplitude. (a) A chip is brought nearby a pattern and ready to be released, (b) the chip is aligned with the pattern. Upper right corner shows that the jagged edge is not fully wetted, which causes misalignment. (c) A chip is brouught nearby extremely jagged pattern and is ready to be released, (d) the chip is aligned with the pattern regardless of large jaggedness.

Measured accuracies from test samples (figure 59) show that the error increases as jaggedness increases, but similarly as with single defects, the effect on alignment accuracy is smaller than the amplitude of the defects. For example, for 5μm constant jaggedness the error is only 1.2 μm (1.3 μm standard deviation) and rotational error is 1.1° (1.2° standard deviation). It is interesting, that the error is largest for jaggedness 3.2μm and 5 μm, and it decreases noticeably for 15 μm jaggedness.

The experimental results are in contrast with theoretical simulation, as the experiments show that both the mean absolute error and standard deviation of error increase when jaggedness increases. On the contrary, simulation results suggested that alignment accuracy is not affected, but only the restoring force is decreased. However, large standard deviation in experiments shows that the alignment can be as accurate with jaggedness as without. The increase in standard deviation is probably due to the decrease in restoring force, which decreases alignment's tolerance of disturbances.

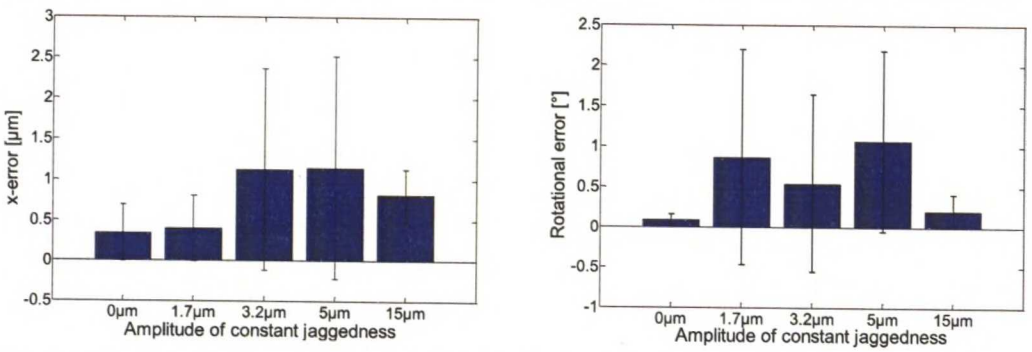

Figure 59: Translational and rotational error with constant edge jaggedness. Values represent mean absolute error with standard deviation errorbars. Each pattern type was tested at least 5 times.

To explain the results in figure 59, the trajectory of the chip on patterns with constant edge jaggedness is simulated in order to find the realistic energy curve. The results in figure 60 show that the edge jaggedness decreases the slope of the energy well, compared to the square pattern. This is in line with Surface Evolver simulation, where restoring force decreases with increasing jaggedness amplitude. This indicates that the alignment reliability is decreased, and therefore some misalignment could be left.

Neither of the Surface Evolver or overlapping models, however, explains why the angular and translational misalignment and standard deviation is smaller for receptor with jaggedness of amplitude of 15 μm than 5 μm and 3.2 μm amplitude. I assume that the reason is the wetting: for amplitudes smaller than 5 μm, the wetting of sharp tips of the jaggedness is more random and therefore usually asymmetric, whereas large jagged features are wetted better and more symmetrically, which reduces the misalignment.

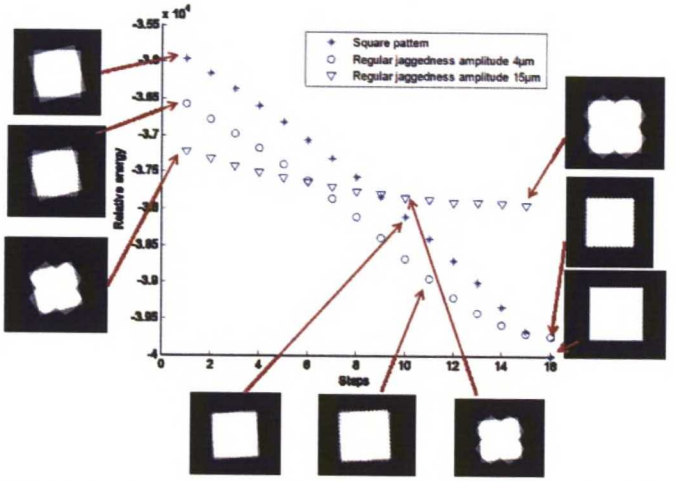

Figure 60: Self-alignment path from 15° twist for square pattern and patterns with constant edge jaggedness. The energy well flattens when the amplitude of the jaggedness increases.

Random edge jaggedness consists of both inward and outward defects with varying area and aspect ratio. The samples with jaggedness 2μm, 4μm and 8μm were tested so that there were at least 5 successful alignments for each jaggedness size. Figure 61 shows one example of a 200 μm × 200 μm SU-8 chip assembled on a 200 μm × 200 μm receptor with random jagged edges of 8 μm amplitude. Table 5 summarizes the simulated alignment accuracies on one pattern for each jaggedness size in section 6.1.1.

Table 5: Examples of alignment accuracy in trajectory simulation

Amplitude	Simulated x-error	Simulated y-error	Simulated twist
2 μm	0 μm	1 μm	0°
4 μm	2 μm	3 μm	0°
8 μm	5 μm	5 μm	1°

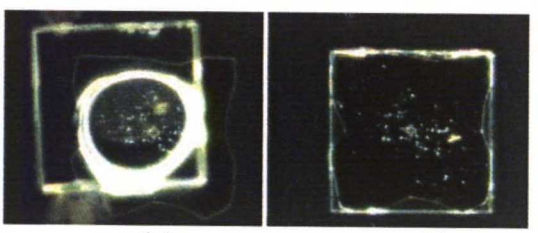

(a) (b)

Figure 61: Self-alignment of a 200μm x 200μm SU-8 chip on a pattern with with random jagged edges of 8μm: a) a chip is brought nearby a pattern and ready to be released, (b) the chip is aligned with the pattern.

The experimental results in figure 62 show that when the amplitude of random edge jaggedness increases, the lateral and rotational misalignment increase, which is also the trend seen in simulation, see table 5. Unlike with constant jaggedness, the increasing trend in misalignment is clear. This shows the difference between constant and random jaggedness: according to simulation, constant jaggedness only lowers the restoring force, but does not alter the energy minimum, whereas random jaggedness also affects the minimum energy position, in addition to the decreased restoring force.

Similar to constant edge jaggedness, the effect on alignment accuracy is smaller than the size of the jaggedness: random jaggedness with 8μm amplitude causes total error 1.4μm ±1μm (1 sigma), which is significantly smaller than simulated 5μm. However, figure 62b shows that rotational error increases dramatically from jaggedness with amplitude of 4μm to 8μm: from 0.5°+/-0.5° to 3°+/-3°. This increase is different from the simulation, where the rotational error is very small also for the largest jaggedness. However, also the standard deviation in experiments is large for largest jaggedness, which is in line with simulated decrease in restoring force with jaggedness.

The sudden increase in rotational error when the jaggedness amplitude is 8μm is probably due to highly distorted shape of the square corners, which greatly affect the shape of the liquid meniscus. With this amount of defects, the self-centering property of self-alignment is still working, but the orientation accuracy decreases.

In conclusion, the comparison of the models to the experimental results shows that simple overlapping method is able to estimate the trend in alignment accuracy for random edge jaggedness, but it overestimates the lateral misalignment (x and y errors) and underestimates the twist. However, the Surface Evolver and overlapping area models for constant edge jaggedness were not able to fully explain the experimental results, which imply that there is a need for models which will take into account the randomness of the wetting.

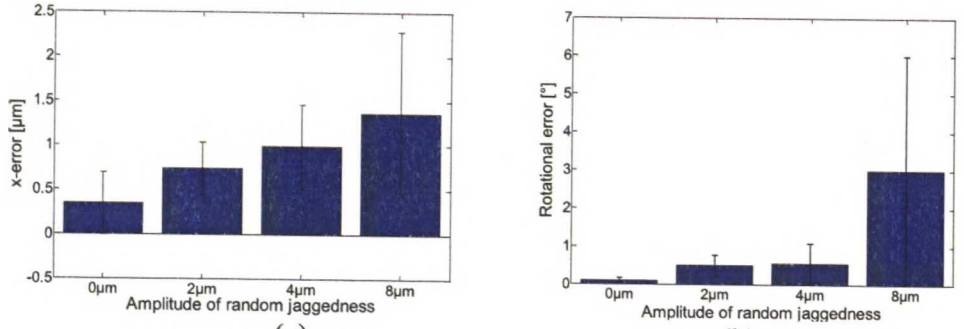

Figure 62: Experimental results of alignment accuracy on patterns with random edge jaggedness. (a) Translational and (b) rotational error with increasing jaggedness amplitude. Values represent mean absolute error with standard deviation errorbars. Each pattern type was tested at least 5 times.

7 Self-alignment failure conditions for topographically confined patterns

In previous sections, liquid was confined to pattern using hydrophilic pads on hydrophobic background. This is needed e.g. when pattern consisted of four pads, all of which should be wetted with one droplet. Then the background must be more hydrophobic than the pattern, because otherwise the liquid may overflow from the gap to outside of the pattern, resulting in failed alignment. However, when the pattern is unbroken, the confinement of the droplet may be easily achieved using solid edge on protruding [15] or recessed [16] patterns. Undercut edges can confine even liquids with very low surface tension to various shapes, provided that the shape does not have segmented parts [50].

In this section the failure condition for overflow on sharp edge of protruding pattern is studied and simple model is created. The model predictions are compared with experimental findings. It should be noted that this does not consider the situation where the droplet has gone over the edge before the chip is released, which may happen due to failed dispensing or too low releasing height, when the gripper pushes the chip so low that droplet is forced to overflow. Thus the precondition is that droplet wets both chip and the pad, and has not overflowed before the chip is released. Figure 63 shows sequence of self-alignment with adhesive, where the pattern edge is not enough for confining the adhesive after the chip is released and the alignment fails due to overflow.

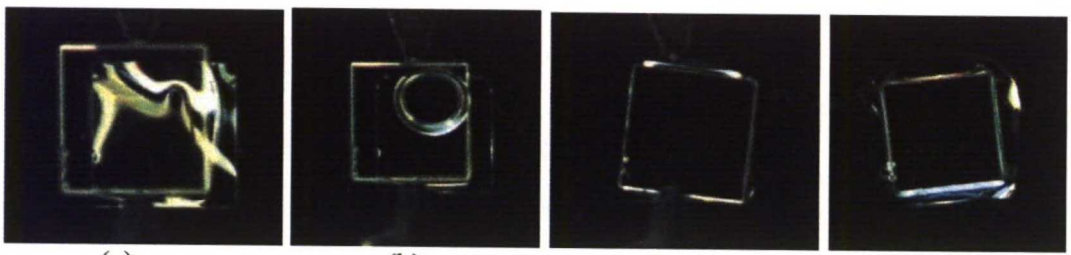

(a) (b) (c) (d)

Figure 63: Silicon pad with adhesive. (a) Chip is brought near. (b) Adhesive droplet wets chip and the pad, no overflow is observed. (c) Chip is released, adhesive starts overflowing. (d) No self-alignment due to overflow.

In addition to that, studying the overflow on topographically confined liquid is interesting, because even with hydrophilic/hydrophobic patterns, the liquid is confined to chip surface by the sharp chip edges. This is because in micro scale the orientation of the whole process does not matter, since gravitation is negligible. In other words, the sharp edge that confines the liquid is also present when the liquid wets the bottom surface of the chip. If the chip edges are not enough for confining the liquid, the chip will be surrounded by the liquid and self-alignment might not be as reliable and accurate as with well-confined liquid.

The most frequent reason of failure in self-alignment is overflow of the liquid over the edge. The analysis of the failure conditions for such confinement is started by considering the configuration illustrated in figure 64. The chip is added on the liquid droplet, which spreads between the chip and the pad and forms liquid meniscus. The

pad edge is sloped, with varying edge angle. Edge angle may vary e.g. due to fabrication process. In the figure 64, θ_{adv_pad} is the advancing contact angle on pad and the θ_{adv_chip} and θ_{rec_chip} are the advancing and receding contact angles on chip respectively.

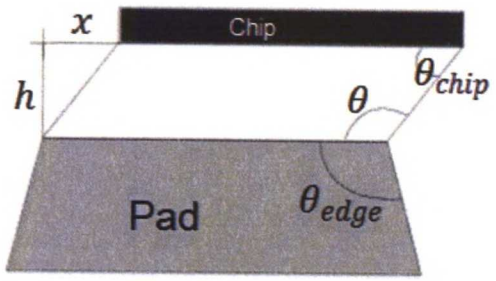

Figure 64: Illustration of derivation of overflow conditions.

The liquid is confined according to Gibb's inequity (2) as long as the angle of the liquid on the edge, θ, has values in range

$$\theta_{adv_{pad}} < \theta < (180° - \theta_{edge}) + \theta_{adv_{pad}} \tag{21}$$

where θ_{edge} is the edge angle, as in figure 64. When the chip is biased, the contact angle that forms between the chip and liquid layer is $\theta_{chip} = 180° - \theta$.

On the other hand, from (2) we get that the overflow happens as soon as the contact angle θ reaches overflow angle:

$$\theta_{overflow} = (180° - \theta_{edge}) + \theta_{adv\_pad}) \tag{22}$$

First assumption to derive the failure conditions is to assume, that overflow can't happen if the liquid starts to dewet the chip before contact angle θ on pad reaches overflow angle. When the receding and advancing contact angle are taken into account, there are two situations that should be considered. Firstly, if the chip is placed on droplet *with bias*, the wetting or dewetting of the chip depends on the advancing contact angle. Thus if $\theta_{chip} < \theta_{adv\_chip}$ when $\theta = (180° - \theta_{edge}) + \theta_{adv\_pad}$ overflow does not happen.

Second case is that the chip is placed *without bias* so that when it is pulled to the side afterwards, the dewetting will happen when chip contact angle reaches receding contact angle on chip. This is more strict condition: if $\theta_{chip} < \theta_{rec\_chip}$ when $\theta = (180° - \theta_{edge}) + \theta_{adv\_pad}$ overflow does not happen.

If the chip dewetting is not taken into account, the bias which will cause overflow of the liquid can be calculated

$$x = \frac{\mathrm{h}}{tan(180° - \theta_{overflow})} = \frac{\mathrm{h}}{tan(\theta_{edge} - \theta_{adv\_pad})} \tag{23}$$

From this we see that if $\theta_{edge} - \theta_{adv\_pad} < 0$ the bias is negative (which is intuitively not meaningful) so the overflow will not happen.

Conditions for successful self-alignment on protruding pattern are then solved:

Overflow will not happen if at least one of the following is true:
Condition (1) $\theta_{edge} < \theta_{adv\_pad}$
Condition (2) $\theta_{edge} < \theta_{adv\_pad} + \theta_{adv\_chip}$ or $\theta_{edge} < \theta_{adv\_pad} + \theta_{rec\_chip}$
Condition (3) $x < \frac{\mathrm{h}}{tan(\theta_{edge} - \theta_{adv\_pad})}$

If none of the above holds, there will be overflow and alignment will fail. In figure 65 the maximum bias, i.e. how far the chip can be pulled without overflow, is plotted with respect of the edge angle from condition (3). In table 6, comparison to experimental observations (see examples of experiments in figures 63 and 66) shows good agreement with the theory. Figure 66 show examples of the experimental observations. Figure 66a shows contact angle of water with silicon oxide, which is typical material in microassembly. In figure 66a the liquid does not overflow when the chip is kept high enough, although the conditions (1) and (2) are not met. After the releasing the chip in figure 66b, the adhesive droplet overflows and alignment fails, as shown in third row of table 6.

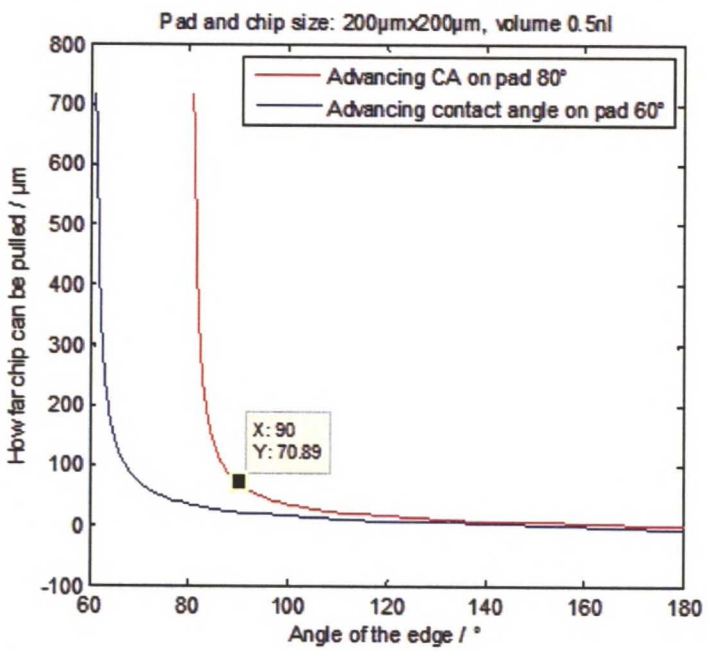

Figure 65: The bias which will result in overflow of liquid in self-alignment experiment on 200 µm × 200 µm pad with 0.5 nl droplet.

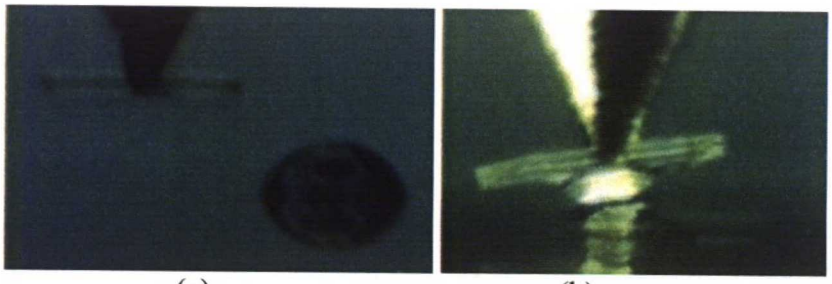

(a) (b)

Figure 66: (a) Silicon pad, covered with native oxide (SiO2) with water droplet on it. Contact angle 70°. (b) Polymer coated SiO2 pads, adhesive droplet. Before releasing, the height is so high that it is possible to pull the chip further, but when the chip is released, overflow happens.

Table 6: Comparison of experimental results with theoretical conditions for overflow

	Pad advancing	Chip receding	Edge angle	Success condition met (estimated h = 12.5 µm)	Overflow or not in the experiments
Polymer coated SiO2 with water	90°	30° (SU-8 chip)	90°	Condition (2) valid, no overflow expected	11/12 no overflow 1/12 overflow, when gripper tips touched the droplet In line with theory
Polymer coated SiO2 with adhesive	< 45°	10-30° (SU-8 chip)	90°	Conditions (1) and (2) not valid. From condition (3) no overflow when x < 12.5µm	1/6 no overflow 5/6 overflow In line with theory
Polymer coated SiO2 with adhesive (UVO114)	65°	10-30° (SU-8 chip)	90°	Condition (2) depends on the contact angle of the chip; if CAs close to 30°, there should be no overflow	11/13: no overflow 2/13 overflow In line with theory
Silicon pad (covered with native SiO2) with water	70°	30°	90°	Condition (2) valid. From condition (3) no overflow when x < 34µm (estimated h = 12.5µm)	3/4 no overflow, 1/4 overflow In line with theory
Silicon pad (covered with native SiO2) with adhesive	50°	10-30°	90°	Conditions (1) and (2) not valid. From condition (3) no overflow when x < 14.9µm	3/3 overflow In line with theory

8 Conclusion

In this thesis, the parameter limits for successful self-alignment were found using modelling, simulation and experiments. The main objective was to study the effect of complex alignment patterns, such as segmented patterns, poorly defined patterns and protruding patterns with different edge angles, on self-alignment. Models were created for these complex patterns, in order to capture the behaviour of the liquid characteristic for those patterns. These numerical models take into account the complete shape of the complex pattern, as well as the partial wetting on the pattern. For comparison, in conventional modelling the pattern is usually assumed circular or square shape, with the presumption that the pattern is wetted fully and the substrate is not wetted at all. It was shown that actually a lot of information about self-alignment reliability and accuracy could be extracted when contact angles on both pattern and substrate are taken into account in self-alignment simulations.

First, the wetting on segmented pattern was studied. Critical volume to wet the segmented pattern sufficiently was found to be linearly dependent on the size of the gap between pattern segments. The results provide a method for approximating droplet volume for segmented four-pad patterns with various sizes and different gaps between the pads. This method could be extended to approximate the volumes needed for segmented patterns with more than four pads, or with different shape. The critical volume was also studied experimentally, and the comparison to theory showed that dynamical factors greatly influence the wetting, for instance, droplet impact on the surface, initial contact point between the droplet and the pattern and dynamics when droplet contacts with the chip. Experimental critical volume was found to be 27 nl, whereas simulated value was 13.4 nl. However, in self-alignment experiments 20 nl turned out to be the best volume for the droplet.

A model for self-alignment on four-pad pattern was created using Surface Evolver program. The model was used to simulate the self-alignment, in order to find the limits for process parameters. It was found that there indeed is a limit for the initial bias, after which the self-alignment becomes more unreliable due to local minimum in system's potential energy. Comparison to experiments, however, showed that the yield of the alignment remains high even with higher biases. In experiments, 100 % yield was observed at 400 µm bias, whereas the simulated upper limit for bias is 365 µm, and the experimental yield was only reduced when bias increased to 500 µm. Then, by using the second, geometry based model to simulate the trajectory of the chip during self-alignment, it was shown that sometimes the alignment may be successful even if the bias is larger than estimated maximum bias, because the chip twists during alignment so that local minimum is avoided.

A simulator was created to simulate the trajectory of the chip from the initial bias to the end position. In this work, the simulator was used to simulate the trajectory of square chip aligning on square pad, segmented pattern and jagged patterns. On the other hand, the simulator allows drawing the alignment pattern and the shape of hydrophilic area on the chip, and, therefore, it can be used for simulating and visualizing alignment on various pattern designs. Simulator is based on well-known method for estimating the potential energy landscape, and currently the step-size was fixed to 1 µm in x and y direction and 1° orientation. Comparison to high-speed video frames showed, that simulated trajectory was close to experimental one, with only minor deviations.

However, the simulator could be further improved to take into account the dynamics, for example, using gradient descent method, so that the step size is related to the magnitude of the gradient.

It is important that small defects in the alignment pattern and chip do not hinder self-alignment performance. Therefore the model for self-alignment on poorly defined patterns was created. Simulations for alignment accuracy on patterns with single defects showed that the defects impair the alignment accuracy, but not at the critical extent for final applications: defect with height 30 % and height 60 % of the pattern edge length caused only 2 % translational misalignment.

The trajectory simulation and Surface Evolver model showed that increasing jaggedness on pattern edges decreases the restoring force. In addition, trajectory simulation predicted increasing misalignment with increasing jaggedness. However, neither of the models was able to explain the better alignment accuracy on patterns with largest constant jaggedness compared to smaller jaggedness. Constant jaggedness of 15 μm amplitude resulted in misalignment of 0.8 μm ± 0.3 μm and 0.2° ± 0.2° twist, whereas 5 μm amplitude caused 1.1 μm ± 1.3 μm lateral error and 1° ± 1.1° twist. The reason is presumably in more deterministic wetting of the pattern with 15 μm jaggedness. This could be further investigated in order to find the optimal size for functional features on the alignment pattern, so that they do not affect the self-alignment accuracy.

Finally, self-alignment on another type of pattern for liquid confinement was studied. Since the confinement of the liquid to the alignment pattern can also be achieved using sharp edge, the patterns with different edge angles were studied. The same overflow rules apply also for liquid confinement on the bottom of the chip, because in micro scale the gravity can be neglected. Overflow conditions were derived based on geometry of the pattern edge and the contact angle of the liquid on the pattern material and on the chip bottom surface. Comparison to experimental cases showed good agreement with theoretical prediction for overflow. This model can be used when materials and liquids are chosen for self-alignment process.

In conclusion, various aspects of self-alignment process were modelled, with special interest on more complicated alignment patterns than circles and squares with hydrophilic/hydrophobic patterning. It was shown that successful self-alignment can be achieved for segmented patterns when the bias is smaller than size of one pattern segment, i.e. pad, which is clearly better than for usual flip-chip applications, where the bias can only be as large as half of the size of the one pad. Furthermore, the comparison between experimental and theoretical results showed that model underestimated the alignment success. The effect of defects and jagged edge shape was shown to be smaller than the size of the imperfection, so that accurate alignment of 1 μm ± 0.5 μm is achievable even with ±4 μm (1 sigma) accuracy of the pattern edges. This relaxes the fabrication tolerances for alignment patterns, and may thus reduce manufacturing cost.

References

[1] B. Chang, I. Routa, V. Sariola, and Q. Zhou, "Self-alignment of RFID dies on four-pad patterns with water droplet for sparse self-assembly," *Journal of Micromechanics and Microengineering*, vol. 21, no. 9, p. 095024, Sep. 2011.

[2] M. Mastrangeli, S. Abbasi, C. Varel, C. Van Hoof, J.-P. Celis, and K. F. Böhringer, "Self-assembly from milli- to nanoscales: methods and applications.," *Journal of micromechanics and microengineering : structures, devices, and systems*, vol. 19, no. 8, p. 83001, Jul. 2009.

[3] B. A. Grzybowski, N. Bowden, F. Arias, H. Yang, and G. M. Whitesides, "Modeling of Menisci and Capillary Forces from the Millimeter to the Micrometer Size Range," *Society*, pp. 404–412, 2001.

[4] V. Sariola, M. Jääskeläinen, and Q. Zhou, "Hybrid microassembly combining robotics and water droplet self-alignment," *IEEE Transactions on Robotics*, vol. 26, no. 6, pp. 965–977, 2010.

[5] R. Fearing, "Survey of sticking effects for micro parts handling," *IEEE International Conference on Intelligent Robots and Systems*, vol. 2, pp. 212–217, 1995.

[6] Z. W. Zhong, T. Y. Tee, and J.-E. Luan, "Recent advances in wire bonding, flip chip and lead-free solder for advanced microelectronics packaging," *Microelectronics International*, vol. 24, no. 3, pp. 18–26, 2007.

[7] V. Sariola, V. Liimatainen, T. Tolonen, R. Udd, and Q. Zhou, "Silicon capillary gripper with self-alignment capability," in *2011 IEEE International Conference on Robotics and Automation*, 2011, pp. 4098–4103.

[8] Q. Zhou and V. Sariola, "Unified view of robotic microhandling and self-assembly," in *Robotic Micro-Assembly*, G. Michaël and S. Régnier, Eds. Ed. Wiley-IEEE Press, 2010, pp. 109–143.

[9] W. Zesch, M. Brunner, and A. Weber, "Vacuum tool for handling microobjects with a NanoRobot," in *Proceedings of International Conference on Robotics and Automation*, 1997, vol. 2, no. April, pp. 1761–1766.

[10] Q. Zhou and P. Korhonen, "Automatic dextrous microhandling based on a 6-DOF microgripper," *Journal of Micromechatronics*, vol. 3, no. 3–4, pp. 359–387, 2006.

[11] P. Lambert and A. Delchambre, "A study of capillary forces as a gripping principle," *Assembly Automation*, vol. 25, no. 4, pp. 275–283, 2005.

[12] C. J. Morris, S. a. Stauth, and B. a. Parviz, "Self-assembly for microscale and nanoscale packaging: steps toward self-packaging," *IEEE Transactions on Advanced Packaging*, vol. 28, no. 4, pp. 600–611, Nov. 2005.

[13] U. Srinivasan, D. Liepmann, and R. T. R. T. Howe, "Microstructure to substrate self-assembly using capillary forces," *Journal of Microelectromechanical Systems*, vol. 10, no. 1, pp. 17–24, Mar. 2001.

[14] K. Sato, K. Ito, S. Hata, and A. Shimokohbeb, "Self-alignment of microparts using liquid surface tension - Behavior of micropart and alignment characteristics," *Precision Engineering*, vol. 27, no. 1, pp. 42–50, Jan. 2003.

[15] C. G. Tsai, C. M. Hsieh, and J. A. Yeh, "Self-alignment of microchips using surface tension and solid edge," *Sensors and Actuators A: Physical*, vol. 139, no. 1–2, pp. 343–349, Sep. 2007.

[16] M. Mastrangeli, W. Ruythooren, C. Van Hoof, and J.-P. Celis, "Conformal dip-coating of patterned surfaces for capillary die-to-substrate self-assembly," *Journal of Micromechanics and Microengineering*, vol. 19, no. 4, p. 045015, Apr. 2009.

[17] Y. Xia, D. Qin, and Y. Yin, "Surface patterning and its application in wetting/dewetting studies," *Current Opinion in Colloid & Interface Science*, vol. 6, no. 1, pp. 54–64, Feb. 2001.

[18] D. Ebert and B. Bhushan, "Durable Lotus-effect surfaces with hierarchical structure using micro- and nanosized hydrophobic silica particles.," *Journal of colloid and interface science*, vol. 368, no. 1, pp. 584–91, Feb. 2012.

[19] B. Chang, A. Shah, I. Routa, H. Lipsanen, and Q. Zhou, "Surface-tension driven self-assembly of microchips on hydrophobic receptor sites with water using forced wetting," *Applied Physics Letters*, vol. 101, no. 11, p. 114105, 2012.

[20] Y. D. Shikhmurzaev, *Capillary Flows with Forming Interfaces*. Taylor & Francis, 2007, pp. 79–83.

[21] H. Gau, S. Herminghaus, P. Lenz, and R. Lipowsky, "Liquid morphologies on structured surfaces: from microchannels to microchips," *Science*, vol. 283, no. 5398, pp. 46–49, Jan. 1999.

[22] J. Berthier, K. Brakke, F. Grossi, L. Sanchez, and L. Di Cioccio, "Self-alignment of silicon chips on wafers: A capillary approach," *Journal of Applied Physics*, vol. 108, no. 5, p. 054905, 2010.

[23] J. W. Gibbs, *Scientific Papers*. London: Longmans, Green & Co, 1906.

[24] N. van Veen, "Analytical Derivation of the Self-Alignment Motion of Flip Chip Soldered Components," *Journal of Electronic Packaging*, vol. 121, no. 2, pp. 116–121, 1999.

[25] K. F. Bohringer, U. Srinivasan, and R. T. Howe, "Modeling of capillary forces and binding sites for fluidic self-assembly," in *14th IEEE Int. Conf. Micro Electro Mechanical Systems*, 2001, pp. 369–374.

[26] M. Mastrangeli, J.-B. Valsamis, C. Van Hoof, J.-P. Celis, and P. Lambert, "Lateral capillary forces of cylindrical fluid menisci: a comprehensive quasi-static study," *Journal of Micromechanics and Microengineering*, vol. 20, no. 7, p. 75041, Jul. 2010.

[27] R. C. Woods, "Development of Analytical Results for the Fluidic Self-alignment Torque on a Silicon Die," *Sensors & Transducers Journal*, vol. 117, no. 6, pp. 71–77, 2010.

[28] K. A. A. Brakke, "Surface Evolver," *Experimental Mathematics*, vol. 1, no. 2, pp. 141–165, 1992.

[29] J. Kim, Y. Shin, and K. Fujimoto, "Dynamic modeling for resin self-alignment mechanism," *Microelectronics Reliability*, vol. 44, no. 6, pp. 983–992, Jun. 2004.

[30] H. Lu and C. Bailey, "Dynamic analysis of flip-chip self-alignment," *IEEE Transactions on Advanced Packaging*, vol. 28, no. 3, pp. 475–480, Aug. 2005.

[31] P. Lambert, M. Mastrangeli, J.-B. Valsamis, and G. Degrez, "Spectral analysis and experimental study of lateral capillary dynamics for flip-chip applications," *Microfluidics and Nanofluidics*, vol. 9, no. 4–5, pp. 797–807, Mar. 2010.

[32] J. Lienemann, A. Greiner, J. G. Korvink, X. Xiong, Y. Hanein, and K. F. Böhringer, "Modeling, Simulation, and Experimentation of a Promising New

Packaging Technology: Parallel Fluidic Self-Assembly of Microdevices," *Sensors Update*, vol. 13, no. 1, pp. 3–43, 2003.

[33] D. T. Schwartz and K. F. Bohringer, "Multi-batch micro-self-assembly via controlled capillary forces," in *Proceedings 2001 IEEE/RSJ International Conference on Intelligent Robots and Systems*, 2001, vol. 3, pp. 1335–1342.

[34] C. Lin, F.-G. Tseng, and C.-C. Chieng, "Orientation-specific fluidic self-assembly process based on a capillary effect," *Journal of Micromechanics and Microengineering*, vol. 19, no. 11, p. 115020, Nov. 2009.

[35] A. Greiner, J. Lienemann, J. G. Korvink, X. Xiong, Y. Hanein, and K. F. Böhringer, "Capillary forces in micro-fluidic self-assembly," in *Technical Proceedings of the 2002 International Conference on Modeling and Simulation of Microsystems*, 2002, pp. 198 – 201.

[36] H. Matsui, Y. Noda, and T. Hasegawa, "Hybrid Energy-Minimization Simulation of Equilibrium Droplet Shapes on Hydrophilic/Hydrophobic Patterned Surfaces.," *Langmuir*, vol. 28, no. 44, pp. 15450–15453, Oct. 2012.

[37] S. A. Stauth and B. A. Parviz, "Modeling of fluidic self-assembly for integration of silicon components on plastic," in *19th IEEE International Conference on Micro Electro Mechanical Systems*, 2006, no. January, pp. 194–197.

[38] D.-A. Wang and B. Liao, "Shaking assisted self-assembly of rectangular-shaped parts," *Journal of Materials Processing Technology*, vol. 210, no. 2, pp. 343–350, Jan. 2010.

[39] J. Dalin, J. Wilde, A. Zulfiqar, P. Lazarou, A. Synodinos, and N. Aspragathos, "Electrostatic attraction and surface-tension-driven forces for accurate self-assembly of microparts," *Microelectronic Engineering*, vol. 87, no. 2, pp. 159–162, Feb. 2010.

[40] B. Chang, M. Jääskeläinen, and Q. Zhou, "Hybrid micro assembly of microchips on segmented patterns," *2010 IEEE International Conference on Automation Science and Engineering*, pp. 15–20, Aug. 2010.

[41] Y. Chan, P. Tu, and K. Hung, "Study of the self-alignment of no-flow underfill for micro-BGA assembly," *Microelectronics Reliability*, vol. 41, no. 11, pp. 1867–1875, Nov. 2001.

[42] C. Lin, F. Tseng, and C.-C. Chieng, "Studies on Size and Lubricant Effects for Fluidic Self-Assembly of Microparts on Patterned Substrate Using Capillary Effect," *Journal of Electronic Packaging*, vol. 130, no. 2, p. 021005, 2008.

[43] K. A. Brakke, "Surface Evolver Manual," 2012. [Online]. Available: http://www.susqu.edu/brakke/evolver/downloads/manual250.pdf.

[44] M. Mastrangeli, W. Ruythooren, J. P. Celis, and C. Van Hoof, "Challenges for capillary self-assembly of microsystems," *IEEE Transactions on Components, Packaging and Manufacturing Technology*, vol. 1, no. 99, pp. 1–1, 2011.

[45] G. Arutinov, E. C. P. Smits, M. Mastrangeli, G. van Heck, J. van den Brand, H. F. M. Schoo, and A. Dietzel, "Capillary self-alignment of mesoscopic foil components for sensor-systems-in-foil," *Journal of Micromechanics and Microengineering*, vol. 22, no. 11, p. 115022, Nov. 2012.

[46] D. E. Goldberg, *Genetic Algorithms in Search, Optimization and Machine Learning*. Reading, MA: Addison-Wesley, 1989.

[47] J. Lienemann, A. Greiner, and J. G. Korvink, "Surface tension defects in microfluidic self-alignment," *Proceedings of SPIE*, vol. 4755, pp. 55–63, 2002.

[48] B. Chang, V. Liimatainen, I. Routa, and Q. Zhou, "High-accuracy positioning of microchips on patterns with jagged edges using hybrid microassembly," *2012 IEEE International Conference on Mechatronics and Automation*, pp. 807–812, Aug. 2012.

[49] B. Chang, M. Jääskeläinen, and Q. Zhou, "Hybrid microassembly of chips on low precision patterns assisted by capillary self-alignment," *2011 IEEE/RSJ International Conference on Intelligent Robots and Systems*, pp. 907–912, Sep. 2011.

[50] V. Liimatainen, V. Sariola, and Q. Zhou, "Controlling Liquid Spreading Using Microfabricated Undercut Edges," *Advanced Materials*, vol. 25, no. 16, pp. 2275–2278, Mar. 2013.